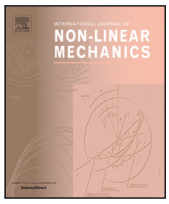
International Journal of Non–Linear Mechanics 191 (2026) 105427



Contents lists available at ScienceDirect

International Journal of Non-Linear Mechanics

journal homepage: www.elsevier.com/locate/nlm



Geometric nonlinear thermo-elastic analysis of thin-walled beams by high-order finite elements

Francesca Bracaglia, Alfonso Pagani *, Enrico Zappino, Erasmo Carrera

Politecnico di Torino, Italy

ARTICLE INFO

Keywords:
Thermo–mechanical analysis
Green Lagrange nonlinearities
Post-buckling analysis

ABSTRACT

Based on the Carrera Unified Formulation (CUF), geometrical nonlinear finite beam elements for the thermo–mechanical analysis of thin-walled structures are presented. The thermomechanical problem is described using a decoupled approach, in which a uniform overtemperature is applied to the beam. Notably, full 3D stress and strain tensor components are considered in the proposed approach as complex distorsions and post-buckling regimes are considered. The nonlinear equations are solved through the finite element method and a Newton–Raphson linearisation scheme. Numerical results include the analysis of Z- and C-section thin-walled metallic beams. After verification, comparisons are made between the full nonlinear and the linearised analyses. The impact of the adopted kinematic theory on the description of the beam nonlinear response and post-buckling is investigated. The analyses highlight that the accuracy of the nonlinear response strongly depends on the theory approximation order when torsional and local modes govern the response. In particular, refined higher-order models are required to obtain a coherent prediction of both the linearised critical modes and the post-buckling equilibrium path.

1. Introduction

Thin-walled structures can be subjected to large elastic distortions under during-life thermal loads, where temperature changes on space structures represent a key loading condition. Differences in temperature due to alternating sunlight exposure and night-time conditions can cause deformations and stresses in space elements. If not considered, these may lead to undesirable structural behaviour. Thermal deformation can affect high-precision elements, such as optical mirrors and reflector antennas [1–3], where stringent tolerances are mandatory. To reduce weight, space applications such as antennas, reflectors, or load-bearing structures frequently use slender and thin components, and beam-type elements are commonly employed [4,5]. These components are prone to large deflections and buckling. In fact, a rise in temperature can induce compressive stress states in thin, restrained, or partially restrained structures. These phenomena under thermal loads must be investigated to avoid excessive deformations. Such deformations could lead to pointing errors or distortion phenomena, for example.

Linear thermo-elastic analyses are widely used for structural investigations, describing displacements and stresses in structures exposed to thermal environments. Hetnarski and Eslami [6] provide a comprehensive treatment of thermoelasticity and equations for linear static thermo–mechanical problems. That work presents beam thermoelastic formulations based on the Euler–Bernoulli (EB) beam theory. Sankar and Tzeng [7] developed a thermoelastic formulation for Functionally Graded (FGM) beams under thermal loading based on a simple Euler–Bernoulli-type beam theory. However, Euler–Bernoulli kinematics neglect transverse shear deformation, which may limit the accuracy of the structural response prediction for short or thick beams. The Timoshenko Beam Theory (TBT) addresses this by allowing beam cross-sections to rotate and accounting for shear effects. This description can be further refined by introducing higher-order theories. The impact of the use of different theories in the linear solution was shown in [8], where classical and higher-order beam models were compared for the a priori approximation of the displacement field over the cross section, with stress and displacement results reported. The book by Carrera et al. [9] presents classical and advanced topics in thermal stress, with a review of the fundamentals and an extension to higher-order theories implemented in the Carrera Unified Formulation (CUF) framework. In all these cases, the theory of linear thermoelasticity is often referenced.

An initial approach to addressing the influence of nonlinearities is to analyse the linearised critical buckling temperature. These analyses are conducted under the assumptions of stable pre-buckling conditions and small to moderate displacements and rotations, allowing for the evaluation of the bifurcation point, which is identified as the critical value at which a sudden change in the shape of the beam

* Corresponding author.
E-mail address: alfonso.pagani@polito.it (A. Pagani).

https://doi.org/10.1016/j.ijnonlinmec.2026.105427
Received 14 May 2026; Received in revised form 30 July 2026; Accepted 5 August 2026
Available online 18 August 2026
0020-7462/© 2026 The Authors. Published by Elsevier Ltd. This is an open access article under the CC BY license (http://creativecommons.org/licenses/by/4.0/).

is expected. Li and Batra [10] investigated analytically the buckling modes and transitions among them of uniformly heated EB beams resting on nonlinear elastic foundations. However, because EB kinematics neglect transverse shear deformation, they may provide less accurate buckling predictions for short beams. Mathew et al. [11] examined the thermal buckling behaviour of antisymmetric cross-ply composite laminates using a shear-deformable structural model. Further contributions on thermal buckling analysis include the work of Yan et al. [12], who investigated the thermal buckling of metallic and laminated beams and plates through a linearised analysis based on total and updated Lagrange formulations. The three-dimensional (3D) equations were obtained using the CUF-improved hierarchical Legendre expansion as a structural basis and the one-dimensional (1D) Finite Element Method (FEM) as a numerical method. Additionally, Derbale et al. [13] conducted a thermo–mechanical buckling analysis of symmetric and antisymmetric laminated composite beams, using a refined higher-order shear deformation theory.

Linear analyses can provide accurate estimates of stresses and displacements at low load levels and can therefore be used as preliminary predictions. On the other hand, under specific loading and geometric conditions, it is necessary to consider the geometrically nonlinear behaviour of beams to describe stresses, displacements, and critical temperatures more accurately. In fact, for slender beams, shell-like structures and structures subjected to non-uniform temperature distribution, the bifurcation-type instability may become questionable, and large deflections have to be taken into account.

The nonlinear response to thermal loads affects slender structures across various applications, including ocean pipes, railway tracks, civil structures, and space antennas. For each application, different studies have been conducted over the years, considering appropriate boundary conditions. For instance in railway tracks and subsea pipelines, which tend to undergo lateral buckling under the hypothesis of elastic or Winkler foundations [10,14,15]. The slender beams used in space applications can be modelled with simply supported or clamped boundary conditions and are often analysed under uniform heating. Basic works on heated rods and beams, under these conditions, were conducted by Li et al. in several studies [16–18]. These studies derived geometrically nonlinear equations for heated rods and beams and solved them using the numerical shooting method to determine the equilibrium path under uniform or transversely non-uniform temperature rises. In [16], an exact mathematical model of an elastic rod with pinned–fixed ends was established based on the Kirchhoff assumption, accounting for the axial extension due to temperature increase. Considering simply supported and clamped beams, the TBT was adopted in [17] to incorporate transverse shear deformation, providing a general formulation exemplified by a pinned–fixed beam. This model was further developed in [18] for pinned–pinned and fixed–fixed beams subjected to transversely non-uniform temperature rises.

Li et al. [19] presented analytical solutions for the thermal post-buckling and vibration responses of symmetric sandwich beams with simply supported and clamped boundary conditions, using a piecewise low-order shear deformation theory. Vaz [20] investigated the initial thermo–mechanical post-buckling behaviour of slender beams subjected to uniform heating, incorporating physical nonlinearity through temperature-dependent material properties and geometrically nonlinear finite displacements. Fu et al. [21], employing first-order shear deformation beam theory, derived governing equations for symmetric laminated composite beams under uniform temperature increases. The study incorporated von Kármán geometric nonlinearity and introduced three solution strategies: the auxiliary function method, the shape function method, and the Ritz method. George et al. [22] conducted both experimental and numerical investigations, employing a nonlinear procedure in commercial software to analyse thermally loaded beams exposed to longitudinal non-uniform temperature profiles. The study validated the influence of temperature fields on the nonlinear buckling behaviour of isotropic beams through experimental analysis. She et al. [23] investigated the thermal buckling and post-buckling of FGM beams under uniform temperature rise by comparing classical EB beam theory, TBT, and higher-order beam theories.

Although the present work focuses on static thermo-elastic post-buckling, recent literature on nonlinear vibration highlights the importance of incorporating higher-order theories for thin-walled structures. Amabili [24] established that for cantilever beams, it is crucial to adopt a proper expansion of the longitudinal displacement that satisfies the natural boundary condition of zero axial force at the tip to ensure convergence and avoid over-predicting nonlinearity. The necessity of a refined third-order shear deformation theory to capture rotary inertia and rotational nonlinearities is also emphasised in [25]. Furthermore, Pagani et al. [26] extended higher-order CUF-based models to nearly incompressible hyperelastic materials, demonstrating that refined fully nonlinear beam models are essential for accurate predictions of local modal phenomena. Liu et al. [27] demonstrated the necessity of an improved high-order finite element framework to efficiently model the rigid–flexible coupling and nonlinear vibrations in rotating systems where large deformations and rotational forces dominate. In the field of mechanical post-buckling and stability, Chen et al. [28] states the importance of using higher-order theories for variable stiffness beams, where the use of EBT with von Kármán nonlinearities is introduced for the description of sandwich skins, while the core needs a more refined theory combined with Green–Lagrange nonlinearities.

To the best of the authors' knowledge, a comparison among kinematic theories in geometrically nonlinear analyses of isotropic beams subjected to thermal loading is still lacking. Existing contributions mainly address displacement-based descriptions of the nonlinear response, the prediction of the critical point, or theory comparisons performed for FGM beams.

This paper proposes a CUF-based methodology to derive the geometrically nonlinear governing equations for beams subjected to thermal loading. The governing equations are obtained using the Principle of Virtual Displacements (PVD) through an FE model developed within the CUF framework. The geometric nonlinearities are accounted for using the full Green–Lagrange strain tensor, and the nonlinear solution is obtained using the path-following method with the arc-length constraint. As demonstrated in various studies and across many applications, including thermo–mechanical analysis [9,29,30], the CUF allows a formulation that remains formally unchanged as the kinematic theory varies. This feature enables a consistent comparison among different kinematic descriptions. Furthermore, the proposed formulation allows an accurate description of the stress field. A comparison between linearised and nonlinear analyses is also carried out to assess the influence of the adopted kinematic theory. Two case studies are considered in the paper: a Z-section beam and a C-section tape spring made of isotropic materials. The choice of these cross-sections is driven by the use of slender beams in space applications, such as stiffeners, antennas, reflectors, and deployable structures. Z-shaped open sections are commonly adopted as stiffening members in lightweight thin-walled structures, while C-shaped sections are representative of tape-spring and deployable boom-like elements [31,32].

The present manuscript is organised as follows. Section 2 presents preliminary information on CUF, FEM implementation, and constitutive equations. Section 3 derives the governing equations for the nonlinear problem, and Section 4 presents the numerical results. Concluding remarks are provided in Section 5.

2. Refined structural beam models

2.1. Carrera Unified Formulation and FEM

The displacement components in the three directions are expressed as in Eq. (1) and constitute the only primary unknowns of the problem.

$$\boldsymbol{u}^T(x,y,z) = \left(u_x, u_y, u_z\right) \tag{1}$$

These displacement components can be written according to CUF as reported in Eq. (2), where the displacement is expressed through the combination of two components. F_τ which represents a set of cross-section expansion functions adopted depending on the structural theory and the 1D *generalised* variables denoted as $\boldsymbol{u}_\tau$ which depends on the beam axis coordinate.

$$\boldsymbol{u}(x,y,z) = F_\tau(x,z)\boldsymbol{u}_\tau(y) \qquad \tau = 1,2,\dots,M \tag{2}$$

where M denotes the dimension of the set of expansion functions, and the use of double subscript indicates summation.

Due to the present formalism, it is possible to obtain different kinematic theories, from classical to higher-order theories, changing the type of function and the order of the expansion functions $F_\tau(x,z)$. In the present paper the Taylor Expansion (TE) functions and Lagrange Expansion (LE) functions will be used. These two classes of functions cover a vast range of classical and high-order theories.

TE models express the cross-section behaviour of the displacement through Taylor-like polynomials defined over th cross-sectional coordinates x and z. The order of the expansion is the polynomial order, and higher-order models are obtained through a hierarchical incrementation of the expansion terms. The adopted Taylor expansion theory is referred to as TEn, where n denotes the order of the expansion. An explicit formulation of TE2 is expressed in Eq. (3).

$$\begin{aligned}
u_x(x,y,z) &= u_{x_1}(y) + xu_{x_2}(y) + zu_{x_3}(y) + x^2u_{x_4}(y) + xzu_{x_5}(y) + z^2u_{x_6}(y)\\
u_y(x,y,z) &= u_{y_1}(y) + xu_{y_2}(y) + zu_{y_3}(y) + x^2u_{y_4}(y) + xzu_{y_5}(y) + z^2u_{y_6}(y)\\
u_z(x,y,z) &= \underbrace{u_{z_1}(y)}_{N=0} + \underbrace{xu_{z_2}(y) + zu_{z_3}(y)}_{N=1} + \underbrace{x^2u_{z_4}(y) + xzu_{z_5}(y) + z^2u_{z_6}(y)}_{N=2}
\end{aligned} \tag{3}$$

where the symbol N here denotes the order of the model and the hierarchical property of this class of function is highlighted. LE models are based on the Lagrangian polynomials, where the unknown functions are the pure displacement components. Lagrange polynomials are usually denoted in terms of natural coordinates. It is possible to use several numbers of nodes in the LE; typically, the LE4, LE9, and LE16 are employed. For Lagrange theory, the notation is LEm, where m denotes the number of nodes on the cross-section. An example of the LE4 function is reported in Eq. (4).

$$\begin{aligned}
u_x &= F_1(x,z)\cdot u_{x_1}(y) + F_2(x,z)\cdot u_{x_2}(y) + F_3(x,z)\cdot u_{x_3}(y) + F_4(x,z)\cdot u_{x_4}(y)\\
u_y &= F_1(x,z)\cdot u_{y_1}(y) + F_2(x,z)\cdot u_{y_2}(y) + F_3(x,z)\cdot u_{y_3}(y) + F_4(x,z)\cdot u_{y_4}(y)\\
u_z &= F_1(x,z)\cdot u_{z_1}(y) + F_2(x,z)\cdot u_{z_2}(y) + F_3(x,z)\cdot u_{z_3}(y) + F_4(x,z)\cdot u_{z_4}(y)
\end{aligned} \tag{4}$$

Details on these models can be found in [30].

Through the FEM the 1D *generalised* displacement is expresses with the shape functions $N_i(y)$ combined with the nodal displacement vector $\boldsymbol{q}_{\tau i}$. Substituting FEM in Eq. (2) it is possible to obtain Eq. (5).

$$\boldsymbol{u}(x,y,z) = F_\tau(x,z)N_i(y)\boldsymbol{q}_{\tau i} \qquad i = 1,2,\dots,N_n \tag{5}$$

where N_n is the total number of finite nodes per element adopted. The explicit form of the vector of nodal displacement is reported in Eq. (6).

$$\boldsymbol{q}_{\tau i}^T = \begin{pmatrix} q_{x_{\tau i}}, & q_{y_{\tau i}}, & q_{z_{\tau i}} \end{pmatrix} \tag{6}$$

A graphical representation of FEM discretisation and expansion functions for the beam model is given in Fig. 1.

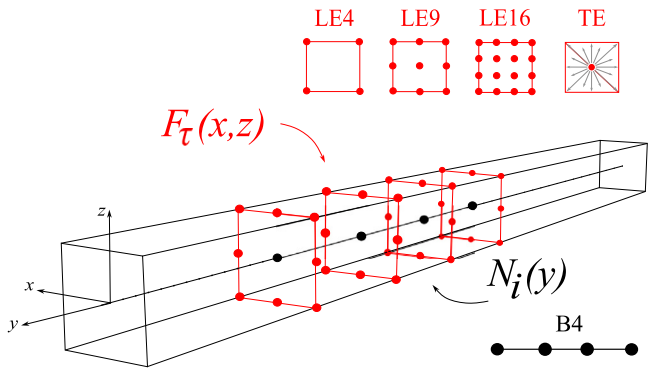


Fig. 1. 1D model, FEM discretisation and CUF expansion theories.

2.2. Constitutive and geometrical relations

The strain $\boldsymbol{\epsilon}$ and the stress $\boldsymbol{\sigma}$ vectors are written in a general form as in Eqs. (7) and (8), respectively. The thermo–mechanical problem is schematised in a decoupled formulation, and strains and stresses can be expressed as two independent vectors: the purely mechanical and thermal vectors.

$$\boldsymbol{\epsilon} = \boldsymbol{\epsilon}_m + \boldsymbol{\epsilon}_\theta = \begin{pmatrix} \epsilon_{xx}, \epsilon_{yy}, \epsilon_{zz}, \epsilon_{xz}, \epsilon_{yz}, \epsilon_{xy} \end{pmatrix}^T \tag{7}$$

$$\boldsymbol{\sigma} = \boldsymbol{\sigma}_m + \boldsymbol{\sigma}_\theta = \begin{pmatrix} \sigma_{xx}, \sigma_{yy}, \sigma_{zz}, \sigma_{xz}, \sigma_{yz}, \sigma_{xy} \end{pmatrix}^T \tag{8}$$

Here, the subscript m denotes the mechanical part, and θ refers to the thermal component. For the following formulation, the temperature is considered uniform all over the beam, and the value of the applied over-temperature does not depend on (x,y,z).

In the present formulation, the geometrically nonlinear behaviour is described by the full 3D Green–Lagrange strain tensor. Within this framework, the second Piola–Kirchhoff stress tensor is adopted, which is work-conjugate to the Green–Lagrange strain tensor. The pure mechanical strains can be written through the geometrical relations reported in Eq. (9).

$$\boldsymbol{\epsilon}_m = \boldsymbol{\epsilon}_l + \boldsymbol{\epsilon}_{nl} = \left(\boldsymbol{b}_l + \boldsymbol{b}_{nl}\right)\boldsymbol{u} \tag{9}$$

where the geometrical differential operator $\boldsymbol{b}$ is divided into its linear ($\boldsymbol{b}_l$) and nonlinear ($\boldsymbol{b}_{nl}$) components. The explicit formulation of the differential operator is reported in Appendix A.

The constitutive equation reported in Eq. (10) establishes the strain–stress relation using the global material properties matrix $\boldsymbol{C}$. The matrix is defined in the Cartesian global reference system whose explicit formulation can be found in the literature [30,33].

$$\boldsymbol{\sigma} = \boldsymbol{C}\boldsymbol{\epsilon} \tag{10}$$

Strains and stresses expressed for the decoupled thermo–mechanical problem are reported in Eq. (11) and Eq. (12), respectively.

$$\boldsymbol{\epsilon} = \boldsymbol{\epsilon}_m + \boldsymbol{\epsilon}_\theta = \boldsymbol{\epsilon}_m - \boldsymbol{\alpha}\Delta\mathcal{T} = \boldsymbol{\epsilon}_l + \boldsymbol{\epsilon}_{nl} - \boldsymbol{\alpha}\Delta\mathcal{T} \tag{11}$$

$$\boldsymbol{\sigma} = \boldsymbol{C}\boldsymbol{\epsilon} = \boldsymbol{C}\left(\boldsymbol{\epsilon}_m + \boldsymbol{\epsilon}_\theta\right) = \boldsymbol{C}\left(\boldsymbol{\epsilon}_m - \boldsymbol{\alpha}\Delta\mathcal{T}\right) = \boldsymbol{\sigma}_m - \boldsymbol{\beta}\Delta\mathcal{T} = \boldsymbol{\sigma}_l + \boldsymbol{\sigma}_{nl} + \boldsymbol{\sigma}_\theta \tag{12}$$

where $\Delta\mathcal{T}$ is the applied over-temperature and $\boldsymbol{\alpha}$ is the vector of the coefficient of thermal expansion whose explicit form is $\boldsymbol{\alpha}^T = (\alpha_1, \alpha_2, \alpha_3, 0, 0, 0)$. The coefficient vector coupling the thermal and mechanical fields is $\boldsymbol{\beta} = \boldsymbol{C}\cdot\boldsymbol{\alpha}$ and is in the form of $\boldsymbol{\beta}^T = (\beta_1, \beta_2, \beta_3, 0, 0, \beta_6)$ with $\beta_6 = 0$ for isotropic materials. Note that the material parameters are considered independent of the temperature. It is possible to incorporate temperature-dependent material properties considering $\boldsymbol{C}(T), \boldsymbol{\alpha}(T)$ and consequently $\boldsymbol{\beta}(T)$, which result in updating these values at each iteration of the nonlinear solution procedure.

3. Nonlinear equations of the thermo-elastic equilibrium

The formulation of the problem under consideration is based on the principle of virtual displacements (PVD) reported in Eq. (13), which imposes equality between the virtual work of the internal forces,

denoted by δL_{int}, and the virtual work of the external load, denoted by δL_{ext}.

$$\delta L_{int} = \delta L_{ext} \tag{13}$$

In this study, we only consider the application of an over-temperature with the exclusion of any external mechanical load which results in $\delta L_{ext} = 0$. However, the formulation can be extended to combined thermo–mechanical loading cases by including the external mechanical load vector through the virtual work of the external forces. Only the virtual internal work needs to be described, and its explicit formulation is as follows:

$$\delta L_{int} = \int_V \delta\boldsymbol{\varepsilon}^T \boldsymbol{\sigma} dV = 0 \tag{14}$$

Substituting Eqs. (7) and (10) into Eq. (14), the virtual internal work becomes:

$$\begin{aligned}\delta L_{int} = \int_V \delta\boldsymbol{\varepsilon}^T \boldsymbol{\sigma} dV &= \int_V \delta\left(\boldsymbol{\varepsilon}_m + \boldsymbol{\varepsilon}_\theta\right)^T \boldsymbol{C}\left(\boldsymbol{\varepsilon}_m + \boldsymbol{\varepsilon}_\theta\right) dV \\ &= \int_V \delta\boldsymbol{\varepsilon}_m^T \boldsymbol{C}\boldsymbol{\varepsilon}_m dV + \int_V \delta\boldsymbol{\varepsilon}_m^T \boldsymbol{C}\boldsymbol{\varepsilon}_\theta dV \\ &= \int_V \delta\boldsymbol{\varepsilon}_m^T \boldsymbol{C}\boldsymbol{\varepsilon}_m dV - \int_V \delta\boldsymbol{\varepsilon}_m^T \boldsymbol{\beta}\Delta\mathcal{T} dV\end{aligned} \tag{15}$$

The virtual variation $\delta\boldsymbol{\varepsilon}_\theta$ is not shown because it is null; in fact, the thermal strains do not change with $\boldsymbol{u}$. The secant stiffness matrix is easily obtained from the first component of Eq. (15) and it consists of four terms expressed in Eq. (16):

$$\int_V \delta\boldsymbol{\varepsilon}_m^T \boldsymbol{C}\boldsymbol{\varepsilon}_m dV = \delta\boldsymbol{q}_{sj}^T \left[\boldsymbol{K}_0^{ij\tau s} + \boldsymbol{K}_{lnl}^{ij\tau s} + \boldsymbol{K}_{nll}^{ij\tau s} + \boldsymbol{K}_{nlnl}^{ij\tau s}\right] \boldsymbol{q}_{\tau i} \tag{16}$$

$\boldsymbol{K}_0^{ij\tau s}$ is the linear component of $\boldsymbol{K}_s^{ij\tau s}$ and coincides with the linear stiffness matrix. $\boldsymbol{K}_{lnl}^{ij\tau s}$ and $\boldsymbol{K}_{nll}^{ij\tau s}$ are the first order nonlinear terms and $\boldsymbol{K}_{nlnl}^{ij\tau s}$ is the second order nonlinear component. The detailed derivation is given in [34], and its explicit form is given in Appendix B. The stiffness matrix is equal to the one defined in the nonlinear mechanical problem since the present formulation is based on a decoupled approach.

The component of the stiffness matrix are expressed in terms of Fundamental Nuclei (FNs), which are the basic components of each matrix or vector. The FNs are formally independent of the order of the structural model or FEM discretisation. The indices i, j are used in the FEM procedure and the indices τ, s are relative to the theory of structures. Thus, the FNs of the stiffness matrices are expressed in terms of four indices, and the FNs of the vectors are written with two indices. To obtain the complete matrix or vector, the building loops on the indices τ, s, i, j are employed. A comprehensive exposition of the FNs and the assembly procedure can be found in Carrera et al. [30].

It is important to note that the matrix $\boldsymbol{K}_s$ is not symmetric. However, there are procedures available to express it in a symmetric form, see [34].

Substituting Eqs. (5) and (9) in the second term of Eq. (15) it is possible to derive the equivalent thermal load vector:

$$\begin{aligned}\int_V \delta\boldsymbol{\varepsilon}_m^T \boldsymbol{\beta}\Delta\mathcal{T} dV &= \int_V \delta\left(\boldsymbol{\varepsilon}_l^T + \boldsymbol{\varepsilon}_{nl}^T\right) \boldsymbol{\beta}\Delta\mathcal{T} dV \\ &= \int_V \delta\boldsymbol{\varepsilon}_l^T \boldsymbol{\beta}\Delta\mathcal{T} dV + \int_V \delta\boldsymbol{\varepsilon}_{nl}^T \boldsymbol{\beta}\Delta\mathcal{T} dV \\ &= \int_V \delta\left(\boldsymbol{b}_l F_s(x,z) N_j(y) \boldsymbol{q}_{sj}\right)^T \boldsymbol{\beta}\Delta\mathcal{T} dV \\ &\quad + \int_V \delta\left(\boldsymbol{b}_{nl} F_s(x,z) N_j(y) \boldsymbol{q}_{sj}\right)^T \boldsymbol{\beta}\Delta\mathcal{T} dV\end{aligned} \tag{17}$$

where τ and i denotes summation over the variable and s and j over variations, see Eq. (5). By applying the differential operator $\boldsymbol{b}$ to the displacement expressed in terms of CUF and FEM as in Eq. (5), it is possible to obtain the algebraic matrix $\boldsymbol{B}$. Furthermore, applying the differential operator, it can be demonstrated that $\delta(\boldsymbol{B}_l^{sj}\boldsymbol{q}_{sj}) = \boldsymbol{B}_l^{sj}\delta\boldsymbol{q}_{sj}$ and $\delta(\boldsymbol{B}_{nl}^{sj}\boldsymbol{q}_{sj}) = 2\boldsymbol{B}_{nl}^{sj}\delta\boldsymbol{q}_{sj}$. The explicit formulation of these matrices is given in Appendix B.

The equivalent thermal load vector $\boldsymbol{F}_\theta$ is obtained from Eq. (17), which can be rewritten as:

$$\begin{aligned}\int_V \delta\boldsymbol{\varepsilon}_m^T \boldsymbol{\beta}\Delta\mathcal{T} dV &= \int_V \delta\boldsymbol{q}_{sj}^T \boldsymbol{B}_l^{sjT} \boldsymbol{\beta}\Delta\mathcal{T} dV + 2\int_V \delta\boldsymbol{q}_{sj}^T \boldsymbol{B}_{nl}^{sjT} \boldsymbol{\beta}\Delta\mathcal{T} dV \\ &= \delta\boldsymbol{q}_{sj}^T \left[\int_V \boldsymbol{B}_l^{sjT} \boldsymbol{\beta}\Delta\mathcal{T} dV + \int_V 2\boldsymbol{B}_{nl}^{sjT} \boldsymbol{\beta}\Delta\mathcal{T} dV\right] \\ &= \delta\boldsymbol{q}_{sj}^T \left[\boldsymbol{F}_{\theta_l}^{sj} + \boldsymbol{F}_{\theta_{nl}}^{sj}\right]\end{aligned} \tag{18}$$

The FNs of the vector of the equivalent thermal load are expressed in Eqs. (19) and (20) (see the equation in Box I).

$$\boldsymbol{F}_{\theta_l}^{sj} = \begin{Bmatrix} \Delta\mathcal{T}\int_V \left[\beta_1 F_{s,x} N_j + \beta_6 F_s N_{j,y}\right] dV \\ \Delta\mathcal{T}\int_V \left[\beta_2 F_s N_{j,y} + \beta_6 F_{s,x} N_j\right] dV \\ \Delta\mathcal{T}\int_V \beta_3 F_{s,z} N_j dV \end{Bmatrix} \tag{19}$$

The load vector is linear in $\Delta\mathcal{T}$ while the nonlinear contribution arises through displacement gradient.

It is possible to rewrite the virtual internal load in Eq. (15) by replacing the secant stiffness matrix reported in Eq. (16) and the thermal load vector from Eq. (18).

$$\begin{aligned}\delta L_{int} = \int_V \delta\boldsymbol{\varepsilon}^T \boldsymbol{\sigma} dV &= \int_V \delta\boldsymbol{\varepsilon}_m^T \boldsymbol{C}\boldsymbol{\varepsilon}_m dV - \int_V \delta\boldsymbol{\varepsilon}_m^T \boldsymbol{\beta}\Delta\mathcal{T} dV \\ &= \delta\boldsymbol{q}_{sj}^T \left[\boldsymbol{K}_0^{ij\tau s} + \boldsymbol{K}_{lnl}^{ij\tau s} + \boldsymbol{K}_{nll}^{ij\tau s} + \boldsymbol{K}_{nlnl}^{ij\tau s}\right] \boldsymbol{q}_{\tau i} \\ &\quad - \delta\boldsymbol{q}_{sj}^T \left[\boldsymbol{F}_{\theta_l}^{sj} + \boldsymbol{F}_{\theta_{nl}}^{sj}\right] = 0\end{aligned} \tag{21}$$

Eq. (21) can be written in a compact form as reported in Eq. (22) which is expressed in terms of FNs.

$$\delta\boldsymbol{q}_{sj}^T : \quad \boldsymbol{K}_s^{ij\tau s}\boldsymbol{q}_{\tau i} - \boldsymbol{F}_\theta^{sj} = 0 \tag{22}$$

The static problem in the assembled form can be written as follows:

$$\boldsymbol{K}_s\boldsymbol{q} - \boldsymbol{F}_\theta = 0 \tag{23}$$

which describes a nonlinear set of equations that cannot be solved directly. Therefore, it is necessary to introduce an incremental linearised scheme. The Newton–Raphson method [35] is employed hereafter, and Eq. (23) can be written as reported in Eq. (24).

$$\boldsymbol{\varphi}_{res} = \boldsymbol{K}_s\boldsymbol{q} - \boldsymbol{F}_\theta \tag{24}$$

The residual nodal forces vector, denoted by $\boldsymbol{\varphi}_{res}$, must be driven to zero to solve the problem.

3.1. Newton–Raphson linearisation scheme

To solve the problem, Eq. (24) is linearised by means of a Taylor's series about the known solution $(\boldsymbol{q}, \Delta\mathcal{T})$. The first-order terms are considered in the expansion, and Eq. (24) becomes as follows:

$$\boldsymbol{\varphi}_{res}(\boldsymbol{q}+\delta\boldsymbol{q}, \Delta\mathcal{T}+\delta\Delta\mathcal{T}) = \boldsymbol{\varphi}_{res}(\boldsymbol{q}, \Delta\mathcal{T}) + \left.\frac{\partial\boldsymbol{\varphi}_{res}}{\partial\boldsymbol{q}}\right|_{\boldsymbol{q}} \delta\boldsymbol{q} + \left.\frac{\partial\boldsymbol{\varphi}_{res}}{\partial(\Delta\mathcal{T})}\right|_{\Delta\mathcal{T}} \delta\lambda(\Delta\mathcal{T})_{ref} = 0 \tag{25}$$

where the thermal load is assumed to be directly linked to the initial thermal loading $(\Delta\mathcal{T})_{ref}$ with a rate of change λ.

The *tangent stiffness matrix* can be defined as $\boldsymbol{K}_T = \left.\frac{\partial\boldsymbol{\varphi}_{res}}{\partial\boldsymbol{q}}\right|_{\boldsymbol{q}}$ and a new thermal load vector called *tangent thermal load vector* it is introduced $\tilde{\boldsymbol{F}}_\theta = -\left.\frac{\partial\boldsymbol{\varphi}_{res}}{\partial(\Delta\mathcal{T})}\right|_{\Delta\mathcal{T}} (\Delta\mathcal{T})_{ref}$ which can be split in two components, a linear and a nonlinear part. Substituting the definitions of the matrix and the new vector, Eq. (25) becomes.

$$\boldsymbol{\varphi}_{res}(\boldsymbol{q}+\delta\boldsymbol{q}, \Delta\mathcal{T}+\delta\Delta\mathcal{T}) = \boldsymbol{\varphi}_{res}(\boldsymbol{q}, \Delta\mathcal{T}) + \boldsymbol{K}_T\delta\boldsymbol{q} - \left(\tilde{\boldsymbol{F}}_{\theta_l} + \tilde{\boldsymbol{F}}_{\theta_{nl}}\right)\delta\lambda = 0 \tag{26}$$

$$\boldsymbol{K}_T\delta\boldsymbol{q} = \tilde{\boldsymbol{F}}_\theta\delta\lambda - \boldsymbol{\varphi}_{res}(\boldsymbol{q}, \Delta\mathcal{T}) \tag{27}$$

$$\boldsymbol{F}^{sj}_{\theta_{nl}} = \begin{Bmatrix} \Delta\mathcal{T} \int_V \left[\beta_1 u_{x,x} F_{s,x} N_j + \beta_2 u_{x,y} F_s N_{j,y} + \beta_3 u_{x,z} F_{s,z} N_j + \beta_6 \left(u_{x,x} F_s N_{j,y} + u_{x,y} F_{s,x} N_j\right)\right] dV \\ \Delta\mathcal{T} \int_V \left[\beta_1 u_{y,x} F_{s,x} N_j + \beta_2 u_{y,y} F_s N_{j,y} + \beta_3 u_{y,z} F_{s,z} N_j + \beta_6 \left(u_{y,x} F_s N_{j,y} + u_{y,y} F_{s,x} N_j\right)\right] dV \\ \Delta\mathcal{T} \int_V \left[\beta_1 u_{z,x} F_{s,x} N_j + \beta_2 u_{z,y} F_s N_{j,y} + \beta_3 u_{z,z} F_{s,z} N_j + \beta_6 \left(u_{z,x} F_s N_{j,y} + u_{z,y} F_{s,x} N_j\right)\right] dV \end{Bmatrix} \tag{20}$$

Box I.

When introducing the loading scale parameter, a new unknown is added to the system, and a new equation must be considered. A general constraint equation is employed to close the problem. The obtained system can be written as follows:

$$\begin{cases} \boldsymbol{K}_T \delta\boldsymbol{q} = \tilde{\boldsymbol{F}}_\theta \delta\lambda - \boldsymbol{\varphi}_{res} \\ c(\delta\boldsymbol{q}, \delta\lambda) = 0 \end{cases} \tag{28}$$

The selection of the constraint equation is pivotal in determining the incremental scheme that will be employed in the numerical solution procedure. The path-following method is defined by acting on both $\delta\lambda$ and $\delta\boldsymbol{q}$. Otherwise, by imposing $\delta\lambda = 0$, a load control method is implemented, and with $\delta\boldsymbol{q} = 0$ a displacement control method is obtained. In the present work, the path-following method introduced by Crisfield [36] and subsequently modified by Carrera [37] is adopted. The implementation of this method in combination with CUF is detailed in [34]. Furthermore, the full Newton–Raphson method is employed, and the tangent matrix and the load vector are updated at each iteration according to the current values of the unknown.

3.2. Derivation of the tangent stiffness matrix

The tangent stiffness matrix is obtained by linearising the virtual strain energy, as reported in Eq. (29).

$$\delta^2 L_{int} = \delta\boldsymbol{q}^T_{sj} \boldsymbol{K}^{ij\tau s}_T \delta\boldsymbol{q}_{\tau i} \tag{29}$$

The application of the virtual variation results into Eq. (30):

$$\delta^2 L_{int} = \delta\left(\int_V \delta\boldsymbol{\varepsilon}^T_m \boldsymbol{\sigma} dV\right) = \int_V \delta\boldsymbol{\varepsilon}^T_m \delta\boldsymbol{\sigma} dV + \int_V \delta^2\boldsymbol{\varepsilon}^T_m \boldsymbol{\sigma} dV \tag{30}$$

The first term of Eq. (30) necessitates the linearisation of the constitutive equations in Eq. (12). It is assumed that the material properties remain constant with respect to the unknown vector $\boldsymbol{q}$. Consequently, the derivative operator is applied only to the strain term in the constitutive equations. It is possible to write Eq. (31).

$$\int_V \delta\boldsymbol{\varepsilon}^T_m \delta\boldsymbol{\sigma} dV = \int_V \delta\boldsymbol{\varepsilon}^T_m \delta(\boldsymbol{\sigma}_m + \boldsymbol{\sigma}_\theta) dV = \int_V \delta\boldsymbol{\varepsilon}^T_m \delta\boldsymbol{\sigma}_m dV + \int_V \delta\boldsymbol{\varepsilon}^T_m \cancel{\delta\boldsymbol{\sigma}_\theta} dV \tag{31}$$

The last term of Eq. (31) is null because the definition of the thermal stress is ($\boldsymbol{\sigma}_\theta = -\beta\Delta\mathcal{T}$), an it does not depend on the unknown of the problem. As a consequence, the first term of Eq. (30) becomes as follows:

$$\int_V \delta\boldsymbol{\varepsilon}^T_m \delta\boldsymbol{\sigma} dV = \delta\boldsymbol{q}^T \left[\boldsymbol{K}_0 + \boldsymbol{K}_{nll} + 2\boldsymbol{K}_{lnl} + 2\boldsymbol{K}_{nlnl}\right] \delta\boldsymbol{q} = \delta\boldsymbol{q}^T \left[\boldsymbol{K}_0 + \boldsymbol{K}_{T1}\right] \delta\boldsymbol{q} \tag{32}$$

$\boldsymbol{K}_{T1}$ represents the nonlinear contribution of the tangent stiffness matrix. However, the components of the tangent matrix appearing in Eq. (32) coincide with those of the secant stiffness matrix. Nevertheless, due to the multiplication factors, the tangent stiffness matrix is symmetric. The explicit formulation of the FNs of the tangent stiffness matrix is reported in Appendix C. Further information on the procedure for obtaining the tangent stiffness matrix for the pure mechanical problem can be found in [34].

The second term of Eq. (30) is expanded in Eq. (33).

$$\int_V \delta^2\boldsymbol{\varepsilon}^T_m \boldsymbol{\sigma} dV = \int_V \cancel{\delta^2\boldsymbol{\varepsilon}^T_l} \boldsymbol{\sigma} dV + \int_V \delta^2\boldsymbol{\varepsilon}^T_{nl} \boldsymbol{\sigma} dV \tag{33}$$

The second variation is applied to the vector $\delta\varepsilon_{nl}$ and acts only on $\boldsymbol{u}$. With some simple manipulations, it is possible to express $\delta^2\boldsymbol{\varepsilon}_{nl}$ vector as the combination of the matrix $\boldsymbol{B}^*_{nl}$ and a vector containing the products of the virtual unknowns. The explicit formulation of the matrix $\boldsymbol{B}^*_{nl}$ is reported in Appendix C. Eq. (33) can now be developed as follows:

$$\begin{aligned} &\int_V \delta^2\boldsymbol{\varepsilon}^T_{nl} \boldsymbol{\sigma} dV = \int_V \left(\boldsymbol{B}^*_{nl} \begin{Bmatrix} \delta q_x \delta q_x \\ \delta q_y \delta q_y \\ \delta q_z \delta q_z \end{Bmatrix}\right)^T \boldsymbol{\sigma} dV \\ &= \int_V \left(\boldsymbol{B}^*_{nl} \begin{Bmatrix} \delta q_x \delta q_x \\ \delta q_y \delta q_y \\ \delta q_z \delta q_z \end{Bmatrix}\right)^T \left(\boldsymbol{\sigma}_l + \boldsymbol{\sigma}_{nl} + \boldsymbol{\sigma}_\theta\right) dV = \\ &\delta\boldsymbol{q}^T \int_V diag\left(\boldsymbol{B}^{*T}_{nl} (\boldsymbol{\sigma}_l + \boldsymbol{\sigma}_{nl} + \boldsymbol{\sigma}_\theta)\right) dV \delta\boldsymbol{q} = \delta\boldsymbol{q}^T \left[\boldsymbol{K}_{\sigma l} + \boldsymbol{K}_{\sigma nl} + \boldsymbol{K}_{\sigma\theta}\right] \delta\boldsymbol{q} \\ &= \delta\boldsymbol{q}^T \left[\boldsymbol{K}_\sigma + \boldsymbol{K}_{\sigma\theta}\right] \delta\boldsymbol{q} \end{aligned} \tag{34}$$

The first two matrices $\boldsymbol{K}_{\sigma l}$ and $\boldsymbol{K}_{\sigma nl}$ are geometric depending on the pure mechanical stress and can be found in literature [34]. The last matrix collects the thermal contributions, and its explicit expression is reported in terms of FN in Eq. (35).

$$\begin{aligned} \boldsymbol{K}^{ij\tau s}_{\sigma\theta} = -\Delta\mathcal{T} \Big(&\beta_1 \int_\Omega F_{\tau,x} F_{s,x} dA \int_L N_i N_j dy \\ &+ \beta_2 \int_\Omega F_\tau F_s dA \int_L N_{i,y} N_{j,y} dy \\ &+ \beta_3 \int_\Omega F_{\tau,z} F_{s,z} dA \int_L N_i N_j dy + \\ &\beta_6 \int_\Omega F_{\tau,x} F_s dA \int_L N_i N_{j,y} dy \\ &+ \beta_6 \int_\Omega F_\tau F_{s,x} dA \int_L N_{i,y} N_j dy \Big) \boldsymbol{I} \end{aligned} \tag{35}$$

Here $\boldsymbol{I}$ denotes the 3 × 3 identity matrix, $dA = dxdz$, Ω is the cross-section, and L is the length of the beam in the y-direction.

The complete form of the tangent stiffness matrix is reported in Eq. (36) and is obtained by combining the contribution given in Eqs. (32) and (34).

$$\begin{aligned} \delta\boldsymbol{q}^T \boldsymbol{K}_T \delta\boldsymbol{q} &= \int_V \delta\boldsymbol{\varepsilon}^T_m \delta\boldsymbol{\sigma} dV + \int_V \delta^2\boldsymbol{\varepsilon}^T_m \boldsymbol{\sigma} dV \\ &= \delta\boldsymbol{q}^T \left[\boldsymbol{K}_0 + \boldsymbol{K}_{T1}\right] \delta\boldsymbol{q} + \delta\boldsymbol{q}^T_{sj} \left[\boldsymbol{K}_{\sigma 0} + \boldsymbol{K}_{\sigma nl} + \boldsymbol{K}_{\sigma\theta}\right] \delta\boldsymbol{q} \\ &= \delta\boldsymbol{q}^T \left[\boldsymbol{K}_0 + \boldsymbol{K}_{T1} + \boldsymbol{K}_{\sigma 0} + \boldsymbol{K}_{\sigma nl} + \boldsymbol{K}_{\sigma\theta}\right] \delta\boldsymbol{q} \end{aligned} \tag{36}$$

3.3. Derivation of the tangent thermal load vector

The tangent thermal load vector is defined as $\tilde{\boldsymbol{F}}_\theta = -\left.\frac{\partial\boldsymbol{\varphi}_{res}}{\partial(\Delta\mathcal{T})}\right|_{\Delta\mathcal{T}}$ $(\Delta\mathcal{T})_{ref}$. Following the definition, the FNs of this vector can be easily obtained as reported in Eq. (37).

$$\tilde{\boldsymbol{F}}_\theta = -\left.\frac{\partial(\boldsymbol{K}_s\boldsymbol{q} - \boldsymbol{F}_\theta)}{\partial\Delta\mathcal{T}}\right|_{\Delta\mathcal{T}} (\Delta\mathcal{T})_{ref} = \left.\frac{\partial(\boldsymbol{F}_\theta)}{\partial\Delta\mathcal{T}}\right|_{\Delta\mathcal{T}} (\Delta\mathcal{T})_{ref} \tag{37}$$

$$\tilde{\boldsymbol{F}}^{sj}_{\theta_{nl}} = (\Delta\mathcal{T})_{ref} \cdot \begin{Bmatrix} \int_V \left[\beta_1 u_{x,x} F_{s,x} N_j + \beta_2 u_{x,y} F_s N_{j,y} + \beta_3 u_{x,z} F_{s,z} N_j + \beta_6 \left(u_{x,x} F_s N_{j,y} + u_{x,y} F_{s,x} N_j\right)\right] dV \\ \int_V \left[\beta_1 u_{y,x} F_{s,x} N_j + \beta_2 u_{y,y} F_s N_{j,y} + \beta_3 u_{y,z} F_{s,z} N_j + \beta_6 \left(u_{y,x} F_s N_{j,y} + u_{y,y} F_{s,x} N_j\right)\right] dV \\ \int_V \left[\beta_1 u_{z,x} F_{s,x} N_j + \beta_2 u_{z,y} F_s N_{j,y} + \beta_3 u_{z,z} F_{s,z} N_j + \beta_6 \left(u_{z,x} F_s N_{j,y} + u_{z,y} F_{s,x} N_j\right)\right] dV \end{Bmatrix} \tag{39}$$

Box II.

Starting from the FNs of the thermal load vector reported in Eqs. (19) and (20), it is easy to obtain the tangent vector nuclei as reported in Eqs. (38) and (39), where linear and nonlinear terms are collected into two vectors (see the equation in Box II).

$$\tilde{\boldsymbol{F}}^{sj}_{\theta_l} = (\Delta\mathcal{T})_{ref} \cdot \begin{Bmatrix} \int_V \left[\beta_1 F_{s,x} N_j + \beta_6 F_s N_{j,y}\right] dV \\ \int_V \left[\beta_2 F_s N_{j,y} + \beta_6 F_{s,x} N_j\right] dV \\ \int_V \beta_3 F_{s,z} N_j dV \end{Bmatrix} \tag{38}$$

It is crucial to consider this additional term in the nonlinear thermo-elastic problem. The nonlinear component, as delineated in Eq. (39), depends on the displacement field. Consequently, it is recommended that a path-following constraint be adopted, since it enables the simultaneous control of both load and displacement parameters to ensure optimal convergence.

4. Numerical results

4.1. Assessment of the numerical model

In the present section, a validation analysis is conducted. The results are compared with those published by Akbas et al. [38]. The beam has a square cross-section; both edges are pinned in the middle line, and a constant over-temperature is applied. The beam is composed of steel whose properties are $E = 210$ GPa, $\nu = 0.27, \alpha = 12.0 \times 10^{-6}$ 1/°C. The dimensions of the beam are defined in terms of L/h, where L is taken to be 1 m, and the cross-section is changed to compare different results to the reference.

Displacement results are taken in Point C in the centre of the beam. Fig. 2 reports the z-direction displacement with respect to the applied over-temperature ΔT. The numerical model consists of 20 4-node beam elements with an LE9 expansion function, and the nonlinearities are described using the full Green–Lagrange strain tensor.

The results in Fig. 2 report a good agreement between the present model and the published ones. The results obtained by analysing the beam with the higher L/h value are in perfect agreement between the two models. On the other hand, when L/h decreases, the results become less similar. This difference could be due to the adopted nonlinear model as well as the order of the kinematic theory. In fact, the reference results are obtained through a von Kármán nonlinearities model using a Timoshenko beam model. By decreasing the slenderness of the beam, the shear effect increases, and the model must be refined.

Fig. 3 reports some results relative to the analysis on the beam with $L/h = 8$. The analyses compare the influence of the nonlinear models and the kinematic model separately to determine which is the main factor affecting the results. The von Kármán nonlinearities are implemented and compared with the full 3D Green–Lagrange strain tensor. In the von Kármán approximation adopted in this work, the nonlinear contribution is restricted to the term $\varepsilon_{yy_{nl}} = \frac{1}{2}\left(\frac{\partial u_z}{\partial y}\right)^2$. It is possible to consider the von Kármán nonlinearities as a simplification of the full Green–Lagrange stain tensor where the only non-null term of the nonlinear matrix reported in Eq. (A.2) is $\boldsymbol{b}_{nl}(2,3)$ [39]. For beams with lower slenderness ratios, transverse shear deformation, finite-rotation effects, and cross-sectional deformation or warping become increasingly significant. Consequently, nonlinear strain components that are neglected by the von Kármán approximation can influence the structural response.

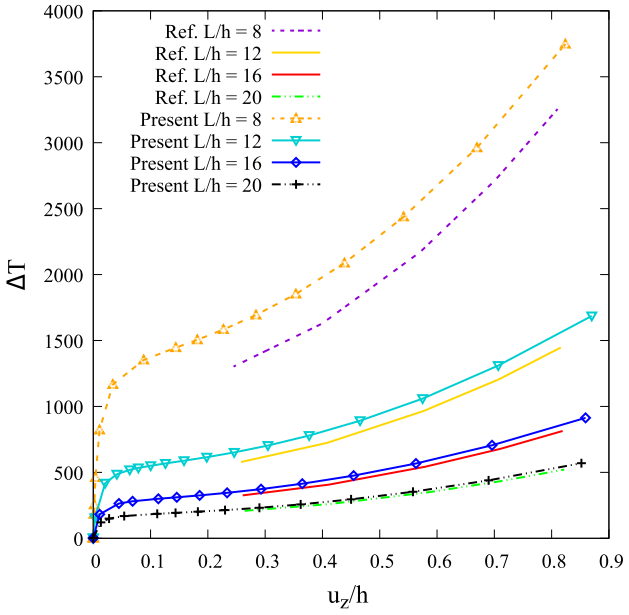


Fig. 2. u_z/h against $\Delta\mathcal{T}$, present method (Green–Lagrange nonlinearities with LE9 expansion theories) compared to Ref. [38] (von Kármán nonlinearities and Timoshenko beam theory). Square-section beam made of steel. Displacement taken in the centre of the beam.

In Fig. 3(a), the same high-order model LE9 is adopted as structural theory, and Green–Lagrange (GL) and von Kármán (VK) nonlinearities are compared. Fig. 3(b) shows the same comparison in terms of nonlinear models employing the TE2 model.

The impact of the two factors is clearly depicted in the graphs. Fig. 3(a) shows that adopting the von Kármán nonlinearities and using the LE9 expansion, the results become closer to the reference, but there is still a considerable difference. Introducing the TE2 expansion and using the von Kármán nonlinearities, the results agree well with the reference. On the other hand, if the TE2 model is chosen with the Green–Lagrange model, the results are similar to the reference, but with a slight difference. The present formulation can replicate the reference model using von Kármán nonlinearities with the TE2 model, as shown in Fig. 3(b). This suggests that at high slenderness, the present model with higher-order-theory and Green–Lagrange nonlinearities gives the same results as the reference, while decreasing the slenderness, the results obtained with this modelling approach start to differ from the reference due to the impact of a difference in both: the description of the kinematics and of nonlinearities. In this condition, agreement with the reference solution is obtained with the TE2-VK model, where the higher-order Green–Lagrange description is expected to provide a more complete description of the problem.

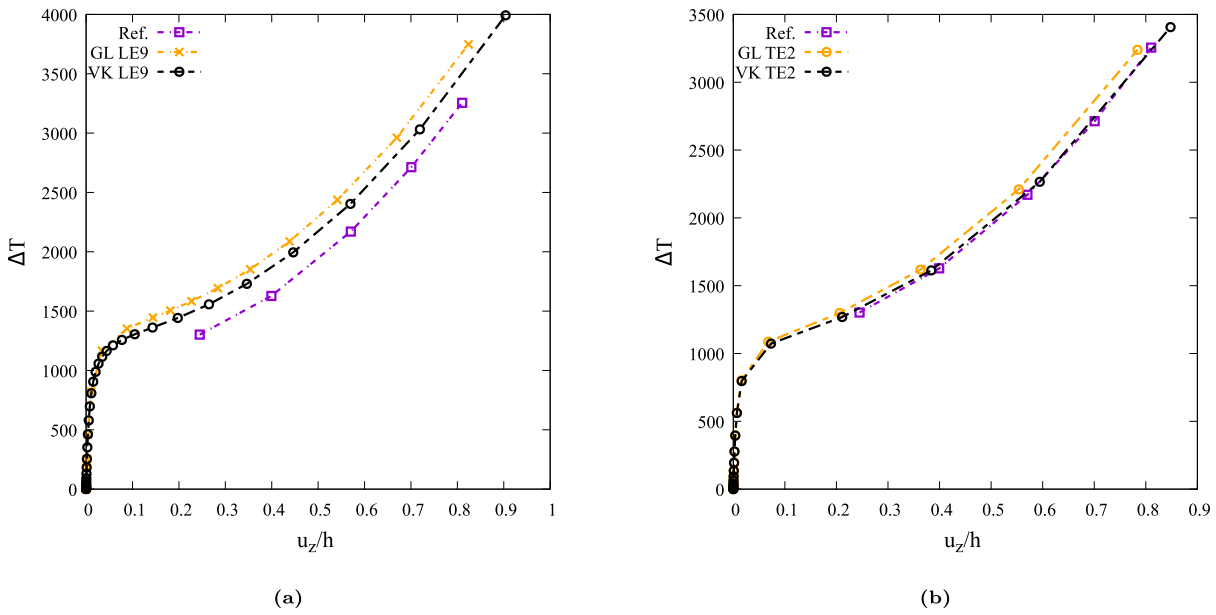


Fig. 3. u_z/h against $\Delta\mathcal{T}$, present model composed of 20 B4 (a) LE9 (b) TE2 expansion function compared to Ref. [38] (von Kármán nonlinearities and Timoshenko beam theory). Comparison between Green–Lagrange (GL) and von Kármán (VK) nonlinearities. Square-section beam made of steel. Displacement taken in the centre of the beam.

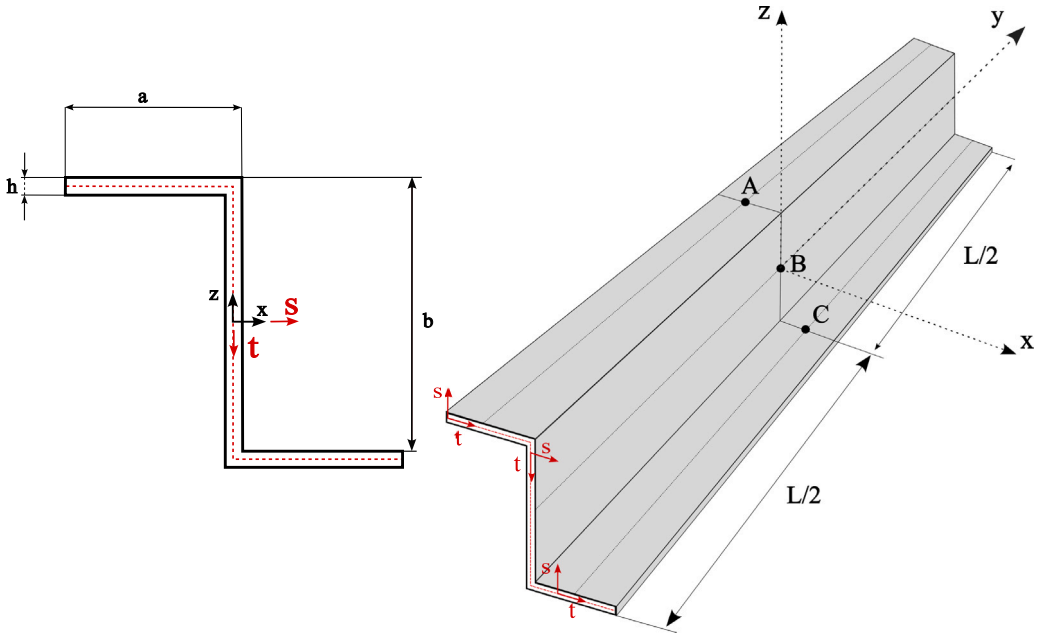


Fig. 4. Geometry of the Z-section beam and representation of the evaluation points. Point A (−a/2, 0, b/2), Point B (0, 0, 0), Point C (a/2, 0, −b/2). (x, y, z) global reference system, (t, s) curvilinear reference system following the middle line of the section.

4.2. Nonlinear thermo–mechanical stresses on z-section beam

In this section, a beam with a z-section is analysed, displacements and stresses are reported and a comparison with the linearised results is presented. The beam is composed of aluminium, whose properties are $E = 75$ GPa, $\nu = 0.3$, $\alpha = 25 \times 10^{-6}/°C$. The beam is $L = 1$ m long, with both edges clamped. Shape and dimensions of the section are depicted in Fig. 4 with $a = 31.5$ mm, $b = 50$ mm and $h = 3$ mm. Furthermore, Fig. 4 shows a curvilinear reference system (t, s) that follows the middle line of the section.

Firstly, a convergence analysis is conducted on the displacements u_x and u_z, and the results are reported for three evaluation points whose coordinates are shown in Fig. 4. The comparison is performed by varying the number of B4 elements along the beam axis. The displacement results are reported in Figs. 5 and 6, where the section expansion theory is kept constant at 66 LE9, whose distribution is reported in Fig. 9. The bifurcation critical temperature is $\Delta T_{cr} = 230$ °C. At such elevated temperatures, a change in material properties is to be expected. However, it is not considered in this study, which is focused on isolating the effect of geometrical nonlinearities; temperature-dependent properties are beyond the scope. Some additional evaluations of the linearised critical temperature compared to the nonlinear results are reported in Fig. 17.

To ensure a good understanding of the results, the displacement values at $\Delta T/\Delta T_{cr} = 1.45$ and 3.7 are reported in Table 1 for the three

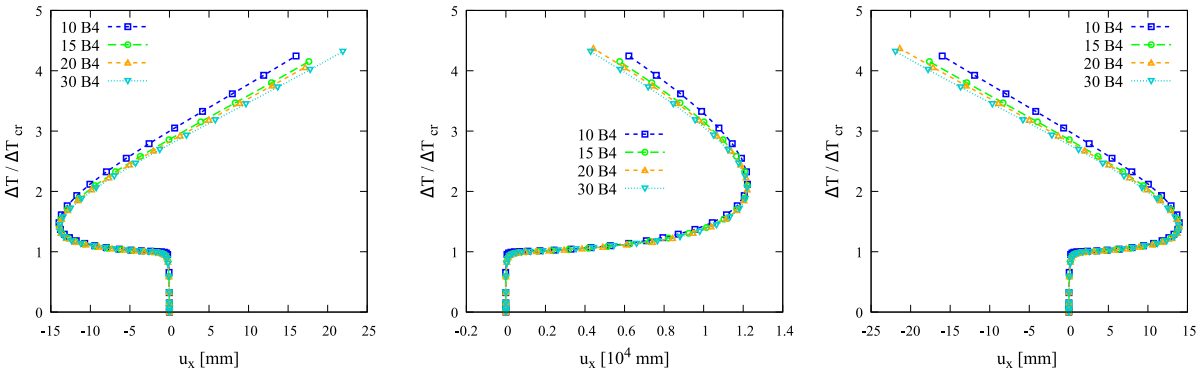


Fig. 5. u_x displacement against $\Delta T/\Delta T_{cr}$, calculated at Points (a) A, (b) B, (c) C. Convergence analysis changing the number of beam elements along the axis with expansion theory fixed at 66LE9. Aluminium Z-section beam with uniform over-temperature and fixed constraints.

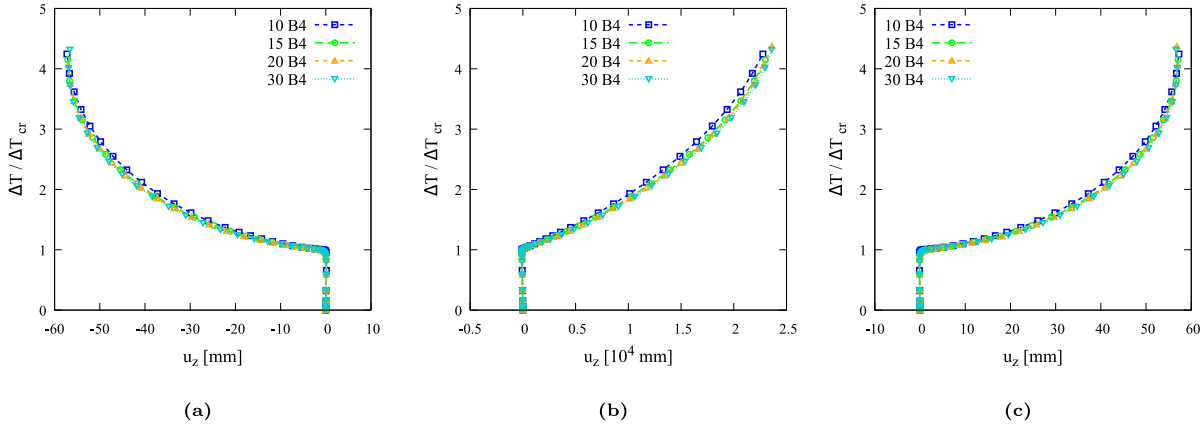


Fig. 6. u_z displacement against $\Delta T/\Delta T_{cr}$, calculated at Points (a) A, (b) B, (c) C. Convergence analysis changing the number of beam elements along the axis with expansion theory fixed at 66LE9. Aluminium Z-section beam with uniform over-temperature and fixed constraints.

Table 1
u_x and u_z displacement at $\Delta T/\Delta T_{cr} = 1.45$ and 3.7, calculated at Points A, B, and C. Convergence analysis changing the number of beam elements along the axis with expansion theory fixed at 66LE9. Aluminium Z-section beam with uniform over-temperature and fixed constraints.

	Point A		Point B		Point C		
	u_x [mm]	u_z [mm]	u_x [mm $\times 10^4$]	u_z [mm $\times 10^4$]	u_x [mm]	u_z [mm]	DOFs
$\Delta T/\Delta T_{cr} = 1.45$							
10B4	−13.96	−26.05	1.04	0.578	13.96	26.05	6136
15B4	−13.93	−26.76	1.01	0.533	13.93	26.76	9108
20B4	−13.90	−27.20	1.04	0.570	13.90	27.20	12 078
30B4	−13.88	−27.15	1.07	0.615	13.88	27.15	18 018
$\Delta T/\Delta T_{cr} = 3.7$							
10B4	9.27	−56.03	0.842	2.102	−9.27	56.03	6136
15B4	12.90	−56.69	0.738	2.194	−12.90	56.69	9108
20B4	12.97	−56.60	0.740	2.192	−12.97	56.60	12 078
30B4	13.09	−56.62	0.729	2.206	−13.09	56.62	18 018

evaluation points. Furthermore, Fig. 7 shows the equilibrium state for the analysis with 30 B4 LE9 at $\Delta T/\Delta T_{cr} = 1.43$, with a scale factor of 1.

As is clear from the results in Figs. 5 and 6, there is a notable difference in the displacement value between the chosen points in the section. The external parts of the beam exhibit larger displacements, and the reason is clearer from the equilibrium state reported in Fig. 7. In fact, the larger displacement is due to torsional effects, which are not negligible given the geometry of the beam. Furthermore, due to the open section of the beam, the torsion is coupled with the warping of the external flanges.

As expected, there is a symmetry in the displacement distribution between the top and bottom flanges due to the symmetry of the problem in terms of load, constraints, and geometry. For the following comparison, vertical segment displacement results are no longer reported because they are low.

The results in Figs. 5 and 6 show that starting from 10B4 elements, the different discretisations are in good agreement in the description of the displacement. Considering a higher load level, with $\Delta T/\Delta T_{cr} = 2$, a slight difference is observed for the 10B4 mesh. Table 1 shows this

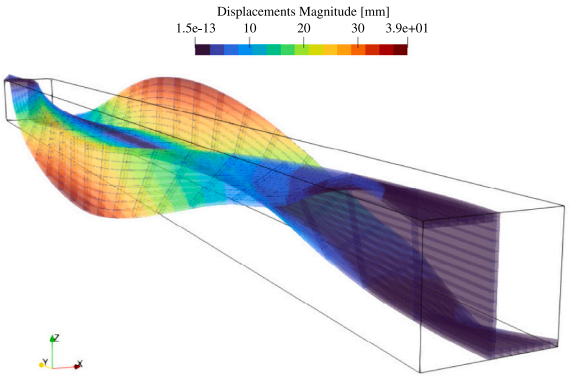


Fig. 7. Equilibrium displacement configuration at $\Delta T/\Delta T_{cr} = 1.43$, scale factor=1. Discretisation with 30B4 along the axis and 66 LE9 expansion theory. Aluminium Z-section beam with uniform over-temperature and fixed constraints.

difference more clearly, where the 10B4 model can capture the displacement at $\Delta T/\Delta T_{cr} = 1.45$ while increasing the over-temperature, the difference in the u_x displacement becomes higher, while the description of u_z remains accurate.

The convergence is also evaluated for the stresses at a high load level ($\Delta T/\Delta T_{cr} = 1.9$) to capture the effects of nonlinearity. In fact, as demonstrated in [40], the convergence of the stresses is highly influenced by the presence of nonlinear phenomena, and a higher level of load necessitates an increase in the discretisation. Fig. 8 reports the stresses along the middle line of the section as indicated by the curvilinear coordinates t and s reported in Fig. 4. The stresses are taken at $y = L/4$.

Fig. 8 represents the convergence of σ_{yy}, and σ_{ty}. The nonlinear analysis shows limited differences for σ_{yy}, and more pronounced variations are observed for σ_{ty}, especially in the regions corresponding to the shear stress peaks. Furthermore, the shear stress distributions satisfy the C_z^0 requirements, with σ_{ty} tending to zero at the free edges of the cross-section. This stress does not vanish, as the study reports the Second Piola–Kirchhoff stress tensor, which is work-conjugate to the Green–Lagrange strain tensor and defined in the undeformed configuration. More details can be found in [41]. Consequently, the reported stress approaches zero without reaching it exactly, since the zero-stress condition needs to be satisfied on the deformed cross-section. The optimum discretisation in terms of beam elements is taken as 20 B4 elements based on the stabilisation of both displacement and stress distributions between successive refinements reported in Figs. 5, 6 and 8.

After defining the optimum number of elements, a first analysis is conducted on the number and distribution of Lagrange elements in the section. This investigation is made only to determine the necessary physical nodes for the Lagrange expansion along the cross-section. Their distribution is depicted in Fig. 9. Different orders of the LE functions are obtained by changing the order of the employed elements, while the best discretisation in terms of the number of elements has to be evaluated by considering their distribution across the cross-section for LE4, LE9, and LE16 to compare these models with the Taylor ones. Fig. 9 reports the distribution of elements along the section. For each distribution, the analysis is conducted using LE4, LE9, and LE16 theories. The linear (LE4), parabolic (LE9), and cubic (LE16) elements have a distribution of physical nodes that is reported in Fig. 1.

The obtained displacements are reported in Fig. 10 and Table 2. Due to the symmetry of the results, clearly shown in Table 1 and Figs. 5 and 6, only the results calculated at Point A are shown. However, for clarity Table 2 reports the displacement for Points A and C taken at $\Delta T/\Delta T_{cr} = 2.2$.

The comparison of the displacements in Fig. 10 obtained with the different discretisations clearly demonstrates that, with the exception

Table 2
u_x and u_z displacement at $\Delta T/\Delta T_{cr} = 2.2$, calculated at Points A and C. Evaluation of the influence of the Lagrange expansion theory on the cross-section changing number and order of LE elements as reported in Fig. 9. Analysis with discretisation fixed at 20B4. Aluminium Z-section beam with uniform over-temperature and fixed constraints.

$\Delta T/\Delta T_{cr} = 2.2$					
	Point A		Point C		
	u_x [mm]	u_z [mm]	u_x [mm]	u_z [mm]	DOFs
5LE4	−9.81	−40.26	9.81	40.26	2196
11LE4	−8.13	−43.06	8.13	43.06	4392
24LE4	−7.68	−43.25	7.68	43.25	9150
31LE4	−7.67	−43.85	7.67	43.85	11 712
66LE4	−7.67	−43.91	7.67	43.91	18 666
5LE9	−7.54	−43.87	7.54	43.87	6039
11LE9	−7.74	−44.01	7.74	44.01	12 627
24LE9	−7.66	−44.01	7.66	44.01	26 901
31LE9	−7.65	−44.00	7.65	44.00	34 587
66LE9	−7.65	−44.00	7.65	44.00	61 305
5LE16	−7.77	−44.10	7.77	44.10	11 712
11LE16	−7.66	−44.04	7.66	44.04	24 888
24LE16	−7.64	−44.00	7.64	44.00	53 436
31LE16	−7.65	−44.00	7.65	44.00	68 808
66LE16	−7.65	−44.00	7.65	44.00	128 100

of the 5LE4 model, all results are accurate in terms of displacement. A slight discrepancy between the models can be observed in the results presented in Table 2. It is evident that, in the case of LE4, even increasing the number of elements in the cross-section leads to less accurate results than discretisations comprising a lower number of LE9 or LE16 elements. The dual impact of the order of expansion and the number of discretisation elements is therefore evident. In terms of displacement, the use of LE9 or LE16 ensures precise results, with the minimum number of elements in the cross-section being 11 for both LE9 and LE16. To assess discretisation quality, it is better to compare stress results from the different models. Figs. 11 and 12 show the stresses along the middle line of the section (as defined in Fig. 4). The value is taken at $y = L/4$.

The stress convergence analysis indicates that a significantly larger number of LE4 elements is necessary to achieve an accurate description of the results. In addition, a mesh with 5LE4 elements provides an inadequate representation of σ_{ty} stress, as it employs linear segments that lack the requisite precision to describe the stress variations along the cross-section.

It is evident that using only five LE4 elements does not provide a satisfactory stress description, whereas higher-order Lagrange expansions, especially LE16, already show a much more stable response with five elements. For LE9 and LE16, the differences with respect to the refined discretisations are significantly smaller and mainly localised in the regions with stronger stress gradients.

However, given the stress distribution, displacements, and DOFs presented in Table 2, a 24LE9 mesh is selected for the following comparison because no significant differences are evident among the subsequent refined models. Now, the best discretisation for the LE model is defined and the following results are reported by changing the class of adopted expansion theory.

The following results present comparisons among different expansion theories, where Taylor models are denoted by TE followed by the number of the polynomial order. More specifically, it will compare results for various orders of TE models with those for converged LE results. A comparison is provided with two FEM models analysed in ABAQUS with two different meshes of C3D8R elements.

The objective of this study is to evaluate the proposed nonlinear geometric model and compare the different expansion models to determine when and whether higher-order models are necessary for the nonlinear analysis of an isotropic beam subjected to thermal loading.

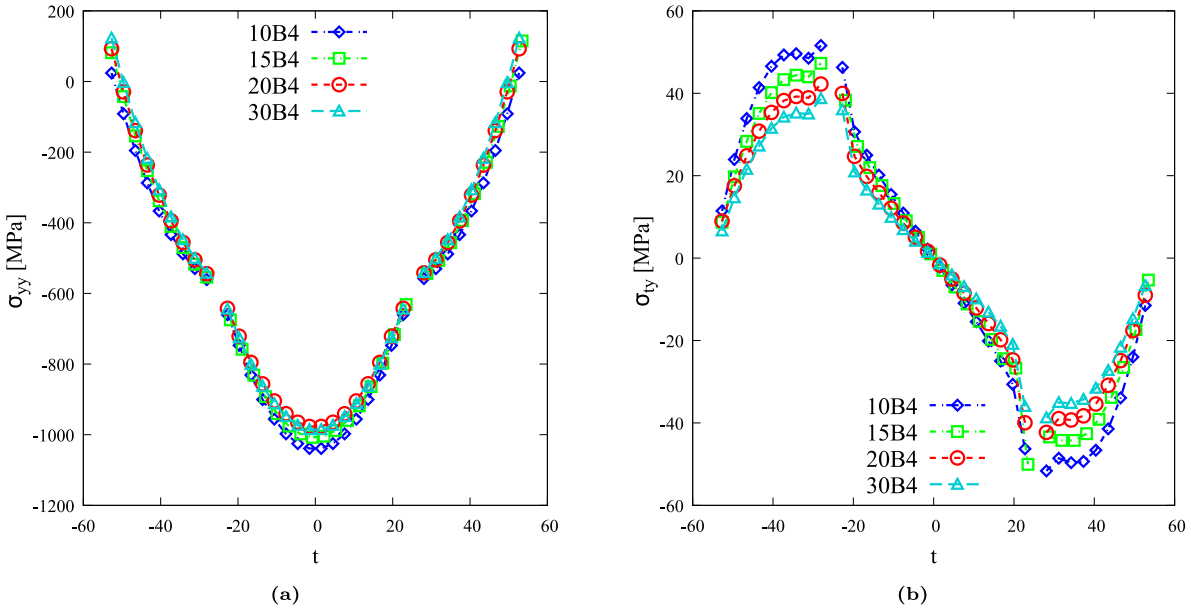


Fig. 8. (a) σ_{yy} and, (b) σ_{ty} against curvilinear coordinate t at $\Delta T/\Delta T_{cr} = 1.9$ calculated at $y = L/4$. Convergence analysis changing the number of beam elements along the axis with expansion theory fixed at 66LE9. Aluminium Z-section beam with uniform over-temperature and fixed constraints.

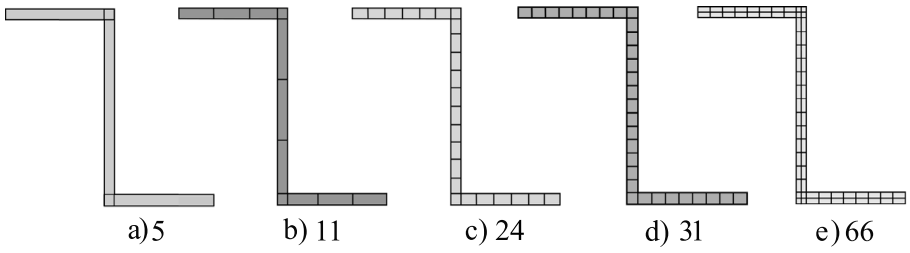


Fig. 9. Lagrange element distribution along the cross-section of the beam.

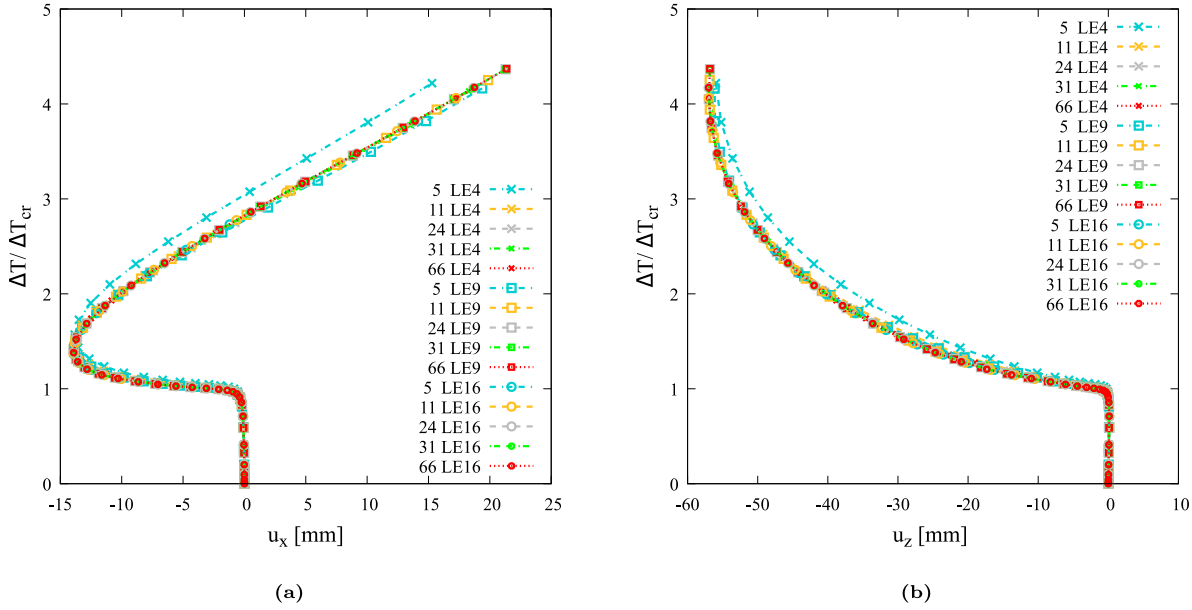


Fig. 10. u_x (a) and u_z (b) displacement against $\Delta T/\Delta T_{cr}$, calculated at Point A. Evaluation of the influence of the Lagrange expansion theory on the cross-section changing number and order of LE elements as reported in Fig. 9. Analysis with discretisation fixed at 20B4. Aluminium Z-section beam with uniform over-temperature and fixed constraints.

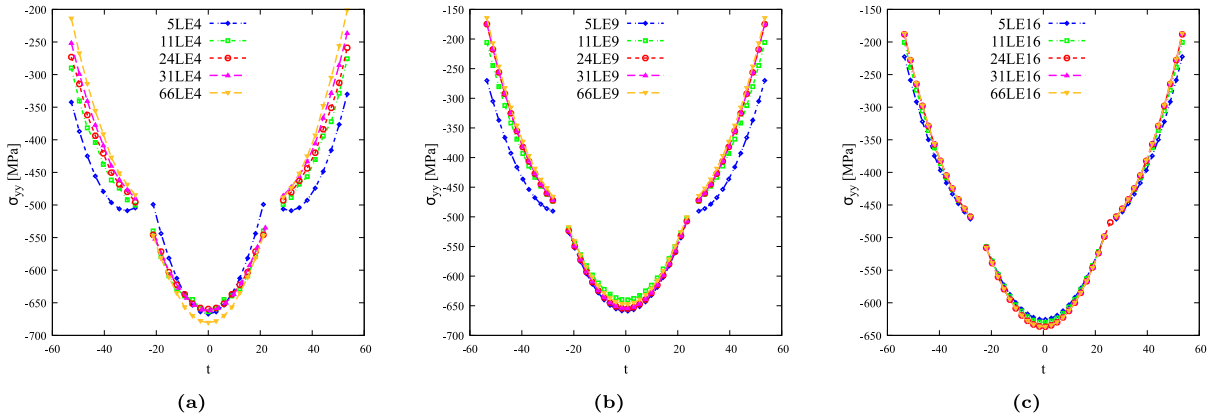


Fig. 11. σ_{yy} against curvilinear coordinate t at $\Delta T/\Delta T_{cr} = 1.3$ calculated at $y = L/4$. Evaluation of the influence of the Lagrange expansion theory on the cross-section changing number and order of LE elements (a) LE4, (b) LE9, (c) LE16. Analysis with discretisation fixed at 20B4. Aluminium Z-section beam with uniform over-temperature and fixed constraints.

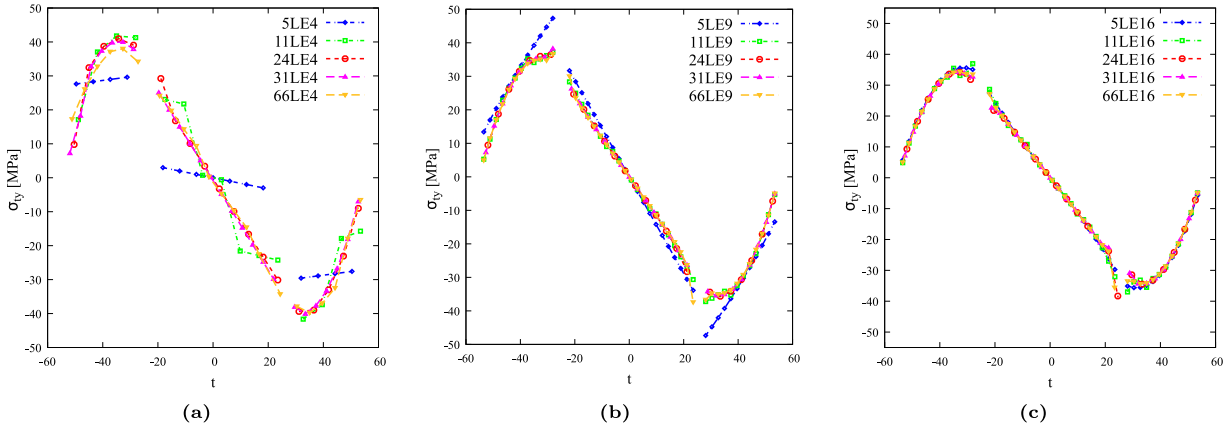


Fig. 12. σ_{ty} against curvilinear coordinate t at $\Delta T/\Delta T_{cr} = 1.3$ calculated at $y = L/4$. Evaluation of the influence of the Lagrange expansion theory on the cross-section changing number and order of LE elements (a) LE4, (b) LE9, (c) LE16. Analysis with discretisation fixed at 20B4. Aluminium Z-section beam with uniform over-temperature and fixed constraints.

Fig. 13 reports the displacement at Point A for different expansion theories, while the ABAQUS A results are reported (see Table 3). The same displacement results at $\Delta T/\Delta T_{cr} = 1.25$ and 1.95 are reported in Table 3 for Points A and C, to ensure the expected symmetry.

In Table 3, two results obtained through two meshes in ABAQUS are reported. Mesh ABAQUS B has the same DOFs as the present LE model, while mesh ABAQUS A is obtained after a convergence analysis. It can be seen that ABAQUS B is not yet convergent, and it appears necessary to employ a model with approximately one order of magnitude more DOFs to obtain results analogous to those from the LE model of the present method. This comparison highlights the main advantages of the CUF formalism, which provides 3D-like results with fewer DOFs than the ABAQUS model. Furthermore, within this formalism, it is possible to compare different expansion theories along the cross-section, ranging from lower- to higher-order models, and to identify the kinematic theory required to describe the thermo-elastic response of beams, including local and warping-related phenomena. For comparison, the equilibrium curve obtained via ABAQUS A has been included in Fig. 13. After comparing the TE4 and TE5 models, only even-order model results are displayed in figures and tables because the results from the even-order model and the subsequent odd-order model are identical.

The curve in Fig. 13 shows that the bifurcation critical temperatures differ depending on the theory used. It is therefore evident that when TE1, TE2, and TE3 models are used no bifurcation point is observed, and the structure does not buckle in the considered temperature range. As the order of the Taylor model increases, from TE4 onwards, a bifurcation point begins to appear; however, it occurs at higher temperatures than those obtained with LE9. As the expansion order increases, the thermal load at which bifurcation occurs decreases until it reaches the value obtained from LE analysis. This underscores the need to employ higher-order Taylor models to determine the nonlinear buckling temperature. The TE8 results show a clear trend toward a higher critical temperature, though the difference from the LE model is slight. The TE10 model yields the same critical temperature as the LE and ABAQUS models.

Table 3 illustrates the displacements for $\Delta T/\Delta T_{cr} = 1.25$ and 1.95 shown for points A and C. It is evident from Fig. 13 that from TE1 to TE6 models have not yet exceeded the bifurcation point for $\Delta T/\Delta T_{cr} = 1.25$, and the relative displacement is very low, while TE8 is just past its critical load and its displacement begins to increase. TE6 is an exception to the trend, which can be attributed to the proximity of the analysed load to the bifurcation point, resulting in the moment of transition from positive to negative displacement being clearly evident. An analysis of the results for $\Delta T/\Delta T_{cr} = 1.95$ facilitates a comparison of the post-buckling behaviour exhibited by the other models. For TE1, TE2, and TE3, the reported displacement is very low because no buckling occurs in this temperature range. Models TE4 and TE5 are just below the critical load, resulting in displacements that are not representative of the post-buckling condition. The models TE6 and TE8 show comparable

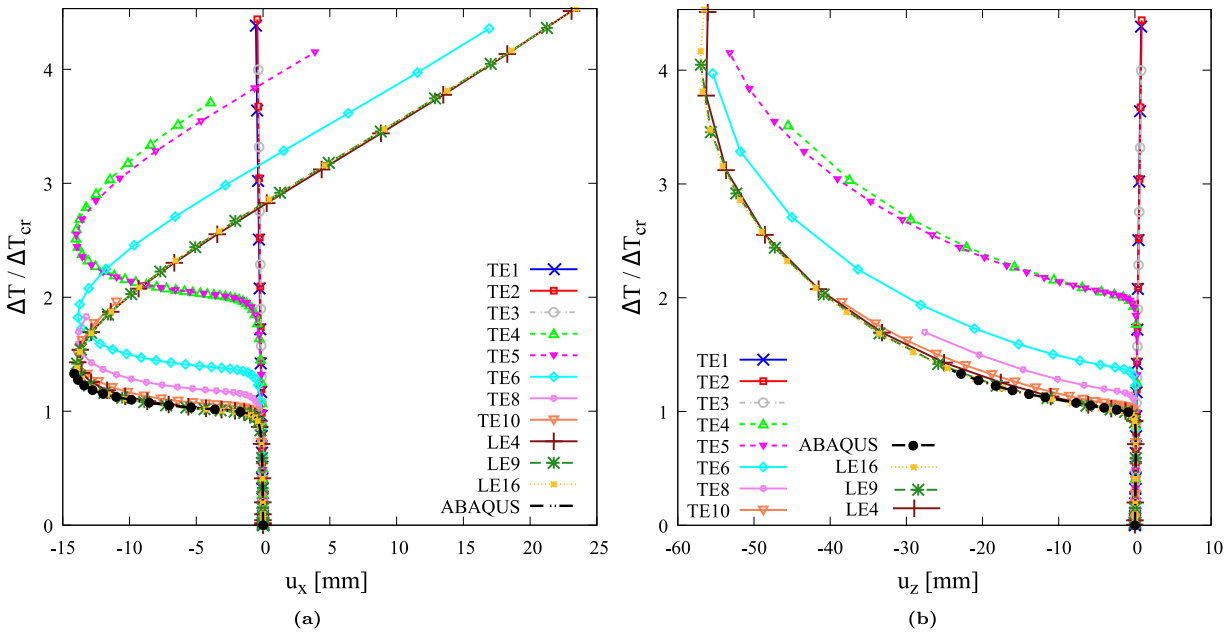


Fig. 13. u_x (a) and u_z (b) displacement against $\Delta T/\Delta T_{cr}$, calculated at Point A. Evaluation of the influence of the Expansion theory comparing TE and LE models. Analysis with discretisation fixed at 20B4. Aluminium Z-section beam with uniform over-temperature and fixed constraints.

Table 3
u_x and u_z displacement at $\Delta T/\Delta T_{cr} = 1.25, 1.95$ calculated at Point A and C. Evaluation of the influence of the Expansion theory comparing TE and LE models. Analysis with discretisation fixed at 20B4. Aluminium Z-section beam with uniform over-temperature and fixed constraints.

	Point A		Point C		
	u_x [mm]	u_z [mm]	u_x [mm]	u_z [mm]	DOFs
$\Delta T/\Delta T_{cr} = 1.25$					
TE1	−0.14	0.22	0.14	−0.22	366
TE2	−0.12	0.24	0.12	−0.24	549
TE3	−0.12	0.27	0.12	−0.27	732
TE4	−0.13	0.25	0.13	−0.25	915
TE5	−0.13	0.27	0.13	−0.27	1098
TE6	−0.47	−0.05	−0.47	−0.05	1281
TE8	−7.01	−5.99	7.01	5.99	1647
TE10	−12.33	−15.72	12.33	15.72	2031
LE9	−13.04	−18.14	13.04	18.14	26 901
ABAQUS A	−13.42	−18.35	13.42	18.35	230 031
ABAQUS B	−15.04	−21.20	15.04	21.20	28 284
$\Delta T/\Delta T_{cr} = 1.95$					
TE1	−0.26	0.39	0.26	−0.39	366
TE2	−0.21	0.42	0.21	−0.42	549
TE3	−0.17	0.39	0.17	−0.39	732
TE4	−1.24	−0.33	1.24	0.33	915
TE5	−1.24	−0.33	1.24	0.33	1098
TE6	−13.72	−28.13	13.72	28.13	1281
TE8	−13.41	−30.80	13.41	30.80	1647
TE10	−10.98	−38.44	10.98	38.44	2031
LE9	−10.65	−39.27	10.65	39.27	26 901

outcomes; however, Fig. 13 indicates that this is attributable only to the load level at which the comparison is made, rather than to an inherent equivalence in the results of the two models. The TE10 model demonstrates superior capacity to represent displacement values, yielding results comparable to those of the LE9 model.

Two types of stress comparisons are reported. The first is in Fig. 14, where the stress results are reported for the different theories at the same displacement level to isolate the stress response associated with comparable deformed conditions. Therefore, the compared configurations are kinematically equivalent but not thermally equivalent, since different temperatures correspond to the same displacement. To

Table 4
Temperature value corresponding to a displacement at Point A $u_x = -12$ mm. Value reported for different expansion theory, displacement taken at $y = L/4$. Z-section Aluminium beam, discretisation 20 B4.

	TE4	TE6	TE8	TE10	LE9
$\Delta T[°C]$	512	366	315	290	270

have a clear understanding of the reported results, Table 4 reports the different temperatures for the same displacement $u_x = -12$ mm. Due to the absence of buckling, TE1 to TE3 results are not reported because they do not reach this displacement. The latter comparison, reported in Fig. 15, is performed with a fixed value of over-temperature to compare the full thermo–mechanical response under the same load level. The results are taken at $y = L/4$.

The stresses shown in Fig. 14 are related to the configuration shown in Table 4, in which the models are compared at a fixed displacement while the corresponding temperature is varied. This implies that the most significant contribution to the difference is expected to be due to the thermal component of the stresses, which is directly linked to the applied over-temperature.

Indeed, Fig. 14 shows that the stresses σ_{yy} exhibit trends across the various results that are almost parallel but shifted, where the TE8, TE10, and LE9 curves show similar trends with different stress levels due to the different thermal loads. Lower-order TE4 and TE6 models exhibit larger discrepancies, with a higher compression state, which may be due to the high over-temperature required to obtain the same displacement value. On the other hand, when considering the shear stress σ_{ty}, the impact of the mechanical component is highlighted, with the thermal contribution being zero from the constitutive relations. In this context, it is interesting to note that, for the same displacement, the mechanical stress component (which, for this shear component, is the only one) obtained via Taylor models differs from the LE9 results. Lower-order TE4 models exhibit pronounced oscillations around the LE9 solution, which become smaller with increasing model order. These results confirm that lower-order models are insufficient to accurately describe the stress field in the configuration under consideration.

Fig. 15 reports the same stresses obtained by comparing the different models at an over-temperature corresponding to $\Delta T/\Delta T_{cr} = 1.7$.

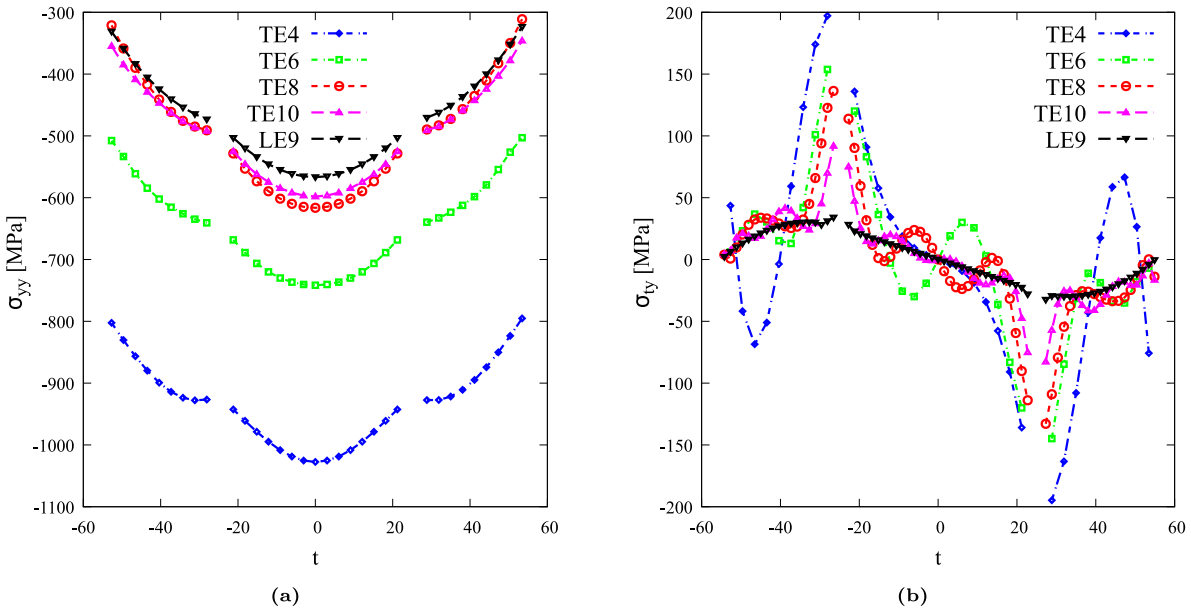


Fig. 14. (a) σ_{yy} and (b) σ_{ty} against curvilinear coordinate t at $u_x = -12$ calculated at $y = L/4$. Corresponding temperature reported in Table 4. Evaluation of the influence of the expansion theory comparing TE and LE models. Analysis with discretisation fixed at 20B4. Aluminium Z-section beam with uniform over-temperature and fixed constraints.

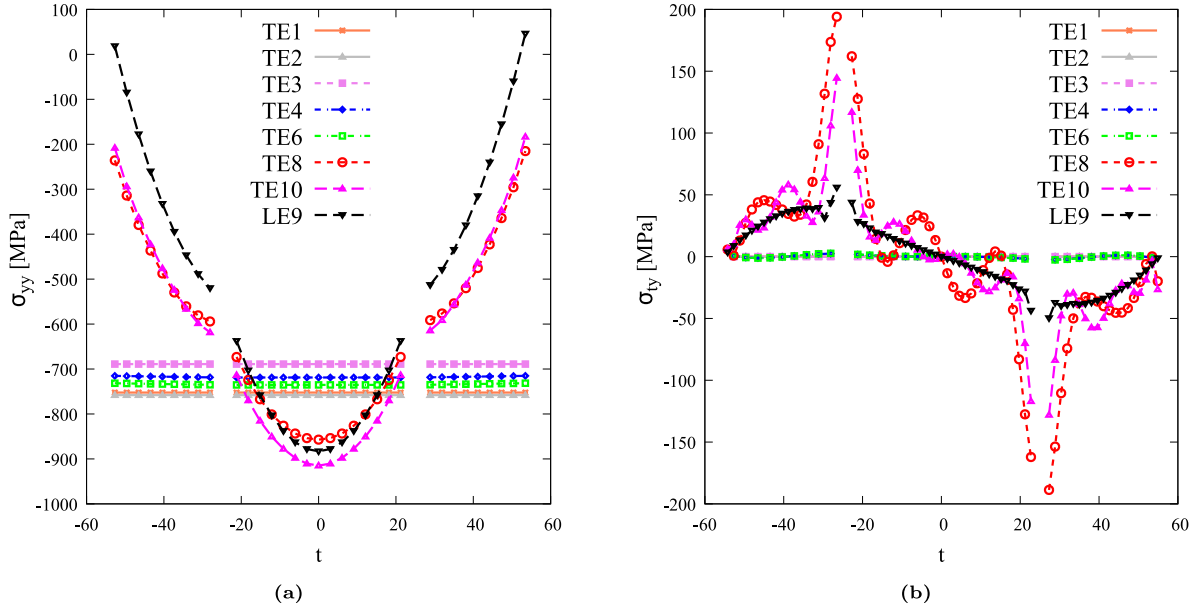


Fig. 15. (a) σ_{yy} and (b) σ_{ty} against curvilinear coordinate t at $\Delta T/\Delta T_{cr} = 1.7$ calculated at $y = L/4$. Evaluation of the influence of the expansion theory comparing TE and LE models. Analysis with discretisation fixed at 20B4. Aluminium Z-section beam with uniform over-temperature and fixed constraints.

In Fig. 15, the lower order models from TE1 to TE6 are unable to reproduce the correct stress distribution for σ_{yy}, which is considered almost constant along the cross-section. It is evident from the displacement in Fig. 13 that at such a temperature, this model describes a deformed configuration that is either in a pre-buckling condition or just after buckling. The TE1 to TE6 models do not allow the shear stress distribution to be described along the cross-section and cannot reproduce the nonlinear variation of the shear stress. TE8 and TE10 models show slight differences from the LE9 results in describing σ_{yy}, but non-negligible discrepancies remain, especially near the external branches of the section. It should also be noted that the TE10 model yields a shear stress distribution close to that of the LE9 model, although local differences are evident in the peak regions. These models tend to describe the LE9 results with some oscillations around the solution.

From these results, it is clear that low-order TE models cannot accurately describe the nonlinear stress redistribution in the beam. This limitation is also consistent with the differences observed in the equilibrium paths.

In order to understand the shear behaviour, which is directly related to the torsional response of the beam, the shear stress field over the cross-section is represented. The transverse shear stress field over the cross-section is represented through the vector composed of the shear stress components σ_{ty} and σ_{ys}. This representation highlights the preferential path and orientation of the shear stresses along the open section. Fig. 16 reports the shear stress along the beam section obtained

Table 5
Linearised buckling critical temperature [°C] for different buckling modes. Evaluation of the influence of the expansion theory comparing TE and LE models. Analysis with discretisation fixed at 20B4. Aluminium Z-section beam with uniform over-temperature and fixed constraints.

Model	1st bending	2nd bending	1st torsional	3rd bending	4th bending	2nd torsional	5th bending
Mode	Fig. 18(a)	Fig. 18(b)	Fig. 18(f)	Fig. 18(c)	Fig. 18(d)	Fig. 18(g)	Fig. 18(e)
	ΔT_{cr} [°C]						
TE1	84.70	172	–	331	493	–	718
TE2	85.80	174	–	337	502	–	734
TE3	85.30	172	–	328	482	–	692
TE4	85.10	171	456	327	479	591	686
TE5	85.00	171	455	326	478	590	684
TE6	85.00	171	314	326	477	455	682
TE7	85.00	171	313	326	477	454	680
TE8	85.00	171	268	325	475	413	–
TE10	85.00	171	230	325	462	391	–
LE9	85.20	171	231	322	–	378	–

with the different theories in the same conditions reported in Fig. 15. The model discretisation is 20B4 along the axis, and the results are taken at $y = L/4$ with $\Delta T/\Delta T_{cr} = 1.7$. The vectors are reported using different scale factors to be clearly visible on the section,while the magnitude of the local shear stress vector is reported in MPa for each graph.

As expected, the lower-order theories cannot accurately describe the transverse shear stress field, which is directly related to the torsional response of the beam. From TE1 to TE3, the shear stress vectors do not reproduce a physically consistent distribution along the open section, since the low-order expansions are unable to describe the nonuniform shear redistribution over the cross-section. Starting from TE4, a more meaningful orientation of the shear stress vectors begins to appear. However, the distribution is still affected by strong local oscillations and does not yet follow the section edges in a fully consistent way. Furthermore, low-order theories cannot represent the magnitude of the shear stress, which is underestimated, with a difference of eight orders of magnitude between TE1 and LE9 results. A more stable shear-stress distribution is obtained with the higher-order models, with TE8 showing the beginning of a consistent pattern and TE10 approaching the LE9 solution. The TE10 distribution approaches the LE9 result, but some local oscillations and deviations remain, especially close to the corners and free edges. The LE9 model provides the most regular representation, with vectors mainly aligned with the walls of the open section.

It is, therefore, useful to report the linearised critical temperatures and buckling modes for the different theories. The complete formulation used to obtain the critical values is presented in [42] and is based on the classical eigenvalue procedure. To facilitate comprehension of the results, the linearised analyses have been summarised and presented in Fig. 17, Table 5, and Fig. 18. The critical temperatures obtained via eigenvalue analyses are reported by comparing the same buckling modes. It has been demonstrated that certain theories are unable to capture certain buckling modes, leading to the absence of corresponding values in the results representation. The absence of certain modes, when the analysis is conducted using different theories, provides interesting insights. As illustrated in Fig. 17, the critical temperatures are categorised into flexural and torsional modes, with the corresponding modes depicted in Fig. 18. The aforementioned description is also incorporated within Table 5 to provide the critical temperature values.

It can be noted that the TE1 first bending temperature is lower than the corresponding one obtained with refined models because a Poisson locking correction is applied through modified material properties that are corrected to improve the solution, as explained in [29].

As shown in Fig. 7, the deformation obtained from the conducted analysis corresponds to the first torsional mode shown in Fig. 18(f). The models TE1 to TE3 fail to describe the torsional mode in both linearised and nonlinear analyses. The lack of accuracy of TE1–TE3 in both the analyses appears to stem from the inability of these low-order models to describe the torsion of this beam. The behaviour of the analysed beam is driven by phenomena such as warping, in-plane deformation, and torsion–bending coupling, which are not generally observed in analyses based on classical theories. For this reason, increasing the expansion order makes the linearised and nonlinear results more coherent in describing the phenomenon, due to the added expansion terms. These refined theories allow an appropriate description of torsion depending on the problem at hand, as demonstrated for linearised analyses in [43].

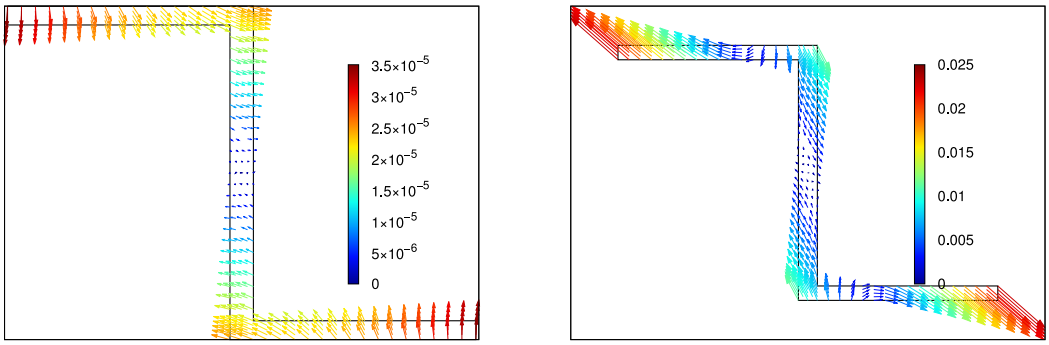
Furthermore, across the other models, it is evident that, from TE4 onwards, a torsional mode begins to emerge; however, its buckling temperature is higher than that obtained with the LE9 model. In particular, this critical value corresponds to the bifurcation point identified in the present nonlinear analysis within the traced equilibrium path. This observation can be extended to the subsequent models, noting that as the TE polynomial order increases, the critical temperature associated with the first torsional mode decreases progressively, tending towards the LE9 value until it matches that of TE10.

It is also evident from the linearised analysis that the torsional mode is not the one associated with the lowest critical temperature. In fact, the linearised analysis yields two flexural modes with almost identical critical temperatures across the different models. However, this mode is not associated with the traced equilibrium path obtained via the present nonlinear analysis, which is focused on the perfect geometry without defects.

4.3. C-section beam

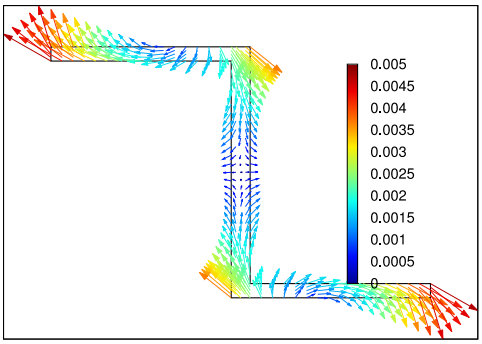
A metallic tape spring with a C-section is considered to further assess the influence of the expansion theories in the presence of open sections with local modes. The geometrical parameters are reported in Fig. 19. The length of the beam is $L = 200$ mm, the thickness is $t = 0.1$ mm, the radius $R = 13.3$ mm, and the angle subtended by the cross-section is $\gamma = 106°$. A linear elastic titanium alloy is considered, with material properties $E = 131$ GPa, $\nu = 0.3$, and $\alpha = 8.7 \times 10^{-6}/°\text{C}$. The beam is clamped at both ends, and a uniform increase in temperature is applied throughout the beam. After a convergence analysis, a mesh of 30 B4 elements is adopted along the beam axis, while the cross-section is represented by 20 LE9 elements.

A preliminary evaluation of the influence of the adopted expansion theory on the linearised buckling load is reported. Table 6 collects the linearised critical temperatures obtained with the different expansion theories. The table is divided into two groups because TE1 and TE2 only capture bending modes, while TE3–TE5 and LE9 capture torsional and local buckling modes. This difference is due to the modes obtained from the linearised analysis. Fig. 20 reports the torsional and local modes, while the bending modes are not reported, as the focus is here on the torsional and local modes governing the nonlinear response.

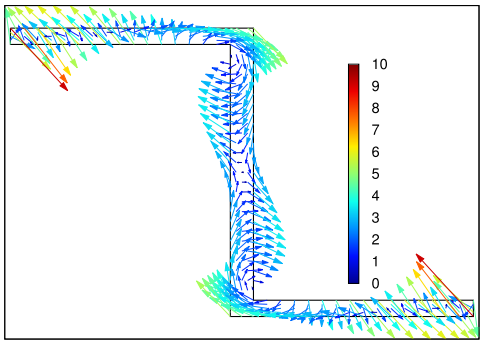


(a) TE1

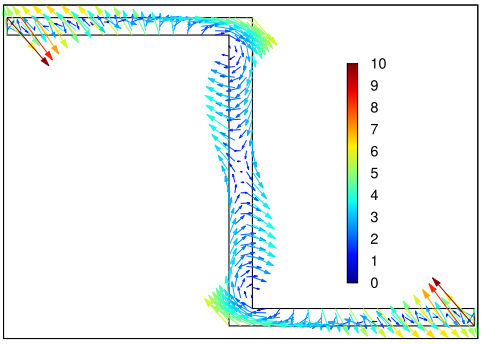
(b) TE2



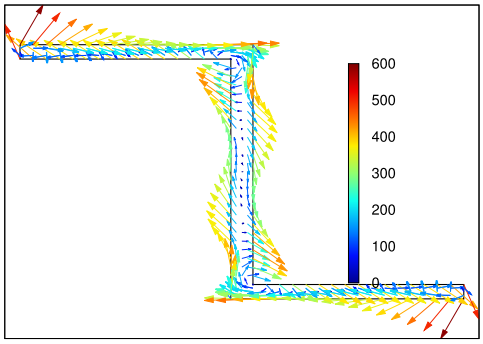
(c) TE3



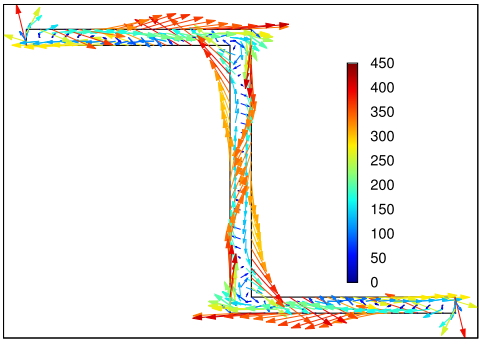
(d) TE4



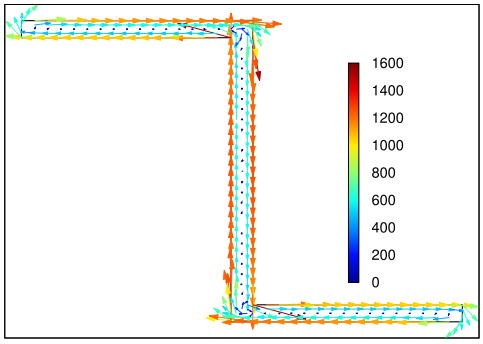
(e) TE6



(f) TE8



(g) TE10



(h) LE9

Fig. 16. Distribution of the vector composed of the shear stress components σ_{ty} and σ_{ys} on the cross-section at $\Delta T/\Delta T_{cr} = 1.7$ calculated at $y = L/4$. Results reported in MPa. Evaluation of the influence of the expansion theory comparing TE and LE models. Analysis with discretisation fixed at 20B4. Aluminium Z-section beam with uniform over-temperature and fixed constraints.

Table 6
Linearised buckling critical temperature [°C] for different buckling modes. Evaluation of the influence of the expansion theory comparing TE and LE models. Analysis with discretisation fixed at 30B4. Titanium alloy C-section beam with uniform over-temperature and fixed constraints. * marks the value which is employed for each expansion theory for the nondimensional results of the nonlinear analysis.

	ΔT_{cr} [°C]						
Model	1st bending	2nd bending	3rd bending	4th bending	5th bending	6th bending	DOF
TE1	297*	600	1153.6	1707.5	2475.8	3220	819
TE2	295*	578	1060.5	1484.5	2010.5	2437	1638
Model	1st torsional	2nd torsional	1st local	2nd local	3rd local	4th local	DOF
Mode	20(a)	20(b)	20(c)	20(d)	20(e)	20(f)	
TE3	48.1	73.42	111.7	111.1*	124.8	127.3	2730
TE4	32.2	58.8	68.9	69.9*	79.3	81.7	4095
TE5	31.4	56.55	55.6	56.0*	66.3	69.95	5733
LE9	31.3	55.7	56.8	57.3*	65.9	68.3	33579

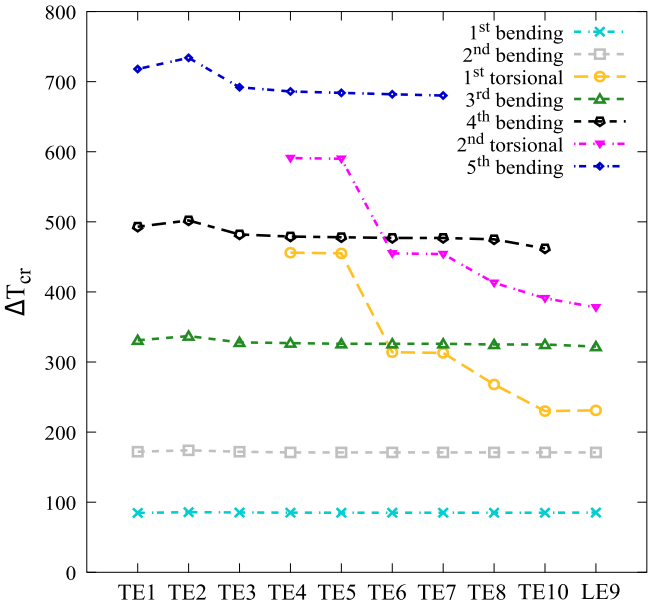


Fig. 17. Linearised buckling critical temperature [°C] for different buckling modes. Evaluation of the influence of the expansion theory comparing TE and LE models. Analysis with discretisation fixed at 20B4. Aluminium Z-section beam with uniform over-temperature and fixed constraints.

Table 6 clearly shows that the transition from TE2 to TE3 is associated with a change in the family of modes captured by the model. From TE3 models onward, this behaviour can be captured, but the critical temperature is higher than that obtained with LE models. It should be noted that, unlike in the previous case, the geometry analysed here features numerous local modes with critical temperatures that are very close to one another. It can also be observed that TE5 and LE9 provide very close critical temperatures for both torsional and local modes. Fig. 21 reports the results of the nonlinear analysis obtained with different expansion theories. The comparison is made in terms of the u_z displacement at the centre of the beam for the nondimensional overtemperature, which is calculated for each theory using the critical temperature marked with * in Table 6. With this normalisation, the bifurcation point is shifted to $\Delta T/\Delta T^*_{cr} = 1$ for each model, allowing a direct comparison of the post-buckling response. Furthermore, the shapes of the deformed beam for the TE1, TE2, and LE9 models are reported in Fig. 22. The numerical value of the displacement for different positions is reported in Table 7, where Point D is in the centre of the beam at y = 0. Point E is located on the point at the edge of the flange at $y = -L/5$, corresponding to the location of maximum displacement in the LE9 solution. Table 7 provides a quantitative comparison of the displacement at representative points of the beam.

Table 7
u_z at point D and u_x and u_z at Point E at $\Delta T/\Delta T^*_{cr} = 1.2$. Temperature value non-dimensionalised using the critical temperature reported in Table 6 with mark *. Evaluation of the influence of the Expansion theory, comparing TE and LE models. Analysis with discretisation fixed at 30B4. Titanium alloy C-section beam with uniform over-temperature and fixed constraints.

	Point D	Point E		
	u_z [mm]	u_x [mm]	u_z [mm]	DOFs
$\Delta T/\Delta T^*_{cr} = 1.2$				
TE1	−3.3819	0.0406	−1.900	819
TE2	2.7581	0.0450	1.6803	1638
TE3	0.3569	0.4020	0.7004	2730
TE4	0.2165	0.3348	0.5129	4095
TE5	0.1654	0.4147	0.5638	5733
LE9	0.1758	0.4525	0.6247	33579

Fig. 21 shows that the displacement obtained using TE1 and TE2 follows a different trend from that of all the other models. On the other hand, TE3-TE5 and LE9 show much closer post-buckling trends, indicating that higher-order theories are able to capture the response more consistently. The graph shows that both, quantitatively and qualitatively, the results between the lower order and higher order theories differ, as can be highlighted by the results in Fig. 22 and Table 7.

In this second geometry as well, it is evident that low-order TE models do not adequately describe local or torsional phenomena, either in linearised or nonlinear analyses. By increasing the order, these phenomena begin to be captured, and the predicted response approaches that obtained with LE9. Given the open-section geometry, the beam is subject to local warping, which is expected to play a significant role and needs to be represented by the adopted kinematics. Furthermore, in this analysed case, unlike the previous one, it is noted that the results are dominated by local phenomena. Based on the comparison between the linearised and nonlinear analyses, the predominant post-buckling mode appears to be related to the second local mode. However, given the proximity of the local linearised modes and their critical temperatures, the post-buckling response may involve multimodal contributions. Unlike the z-section beam, the structural response is characterised by several closely spaced local modes, which have an impact on the post-buckling response. For the higher-order models, the bending critical load is not associated with the modes governing the nonlinear response. In this case, refined kinematics are needed not only for torsion but also for the closely spaced local modes that strongly affect the post-buckling response.

5. Conclusion

A Finite Element Methodology (FEM) implemented within the Carrera Unified Formulation (CUF) was developed for performing nonlinear geometric analyses in response to applied thermal loads. The

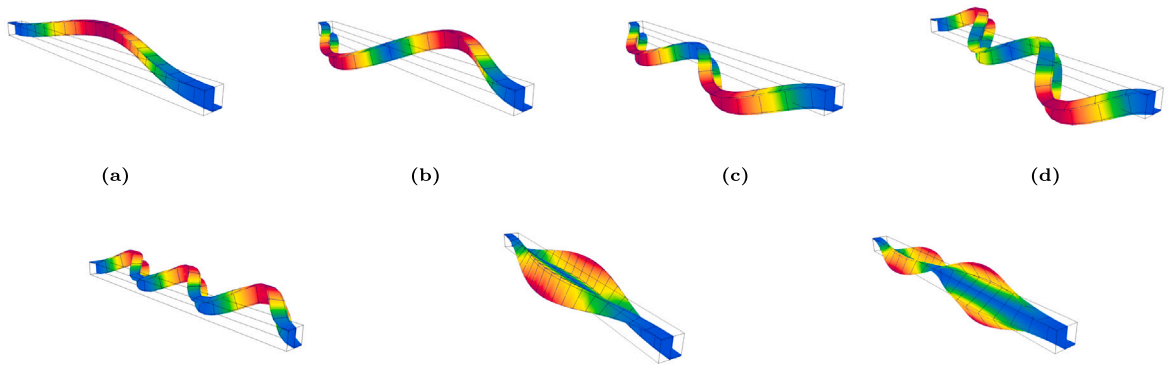


Fig. 18. Linearised buckling critical modes. (a)–(e) bending modes from 1st to 5th, (f) 1st torsional, (g) 2nd torsional. Analysis with discretisation fixed at 20B4. Aluminium Z-section beam with uniform over-temperature and fixed constraints.

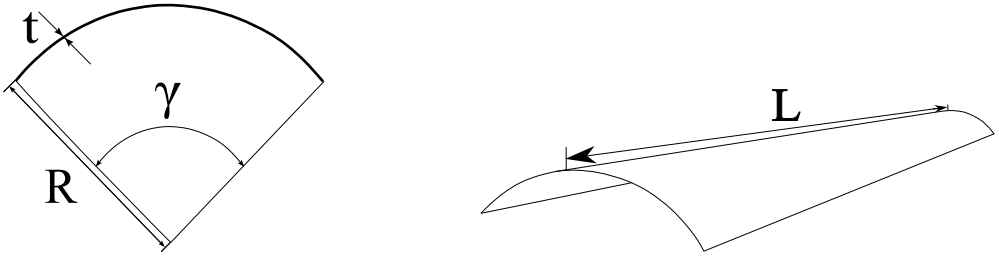


Fig. 19. Geometry of the C-section beam.

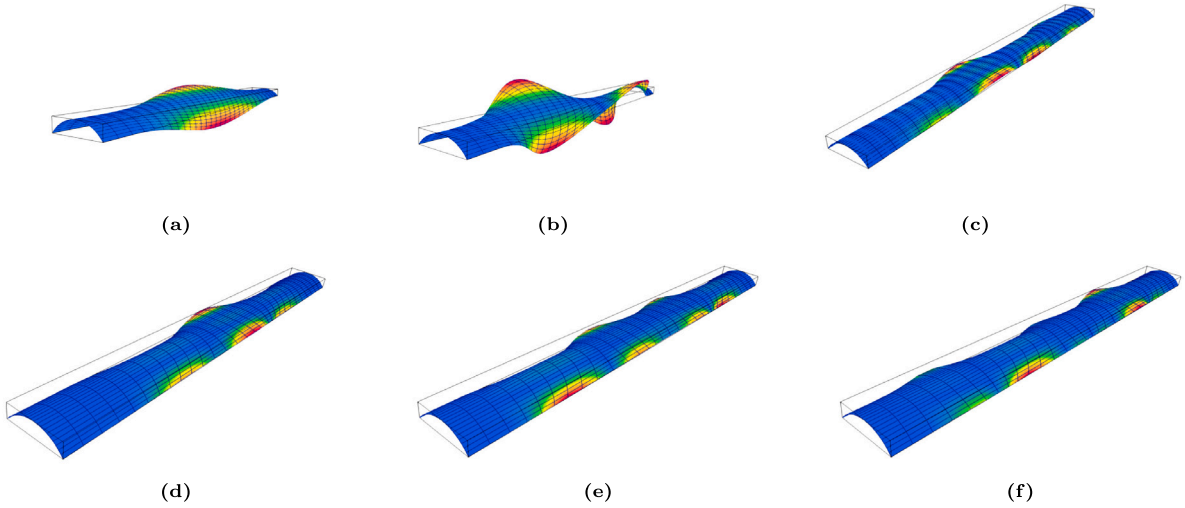


Fig. 20. Linearised buckling critical modes. (a)–(b) 1st and 2nd torsional modes, (c)–(f) local modes. Analysis with discretisation fixed at 30B4. Titanium alloy C-section beam with uniform over-temperature and fixed constraints.

governing equations were derived using the Principle of Virtual Displacement (PVD), and nonlinearities were taken into account through the full strain Green–Lagrange tensor. The analysis accounted for geometric nonlinearities, and the material properties were considered constant along the entire equilibrium curve. The nonlinear model was assumed to be free of initial imperfection in order to evaluate the nonlinear formulation and the ideal behaviour of the beam. Therefore, temperature-dependent material, initial imperfections, and fully coupled or non-uniform thermal fields are outside the scope of the present work.

The solution to the nonlinear system was obtained using the path-following method, in which the arc-length constraint was implemented. In this way, the equilibrium path was traced via an iterative procedure. The CUF allows for the implementation of various kinematic theories through the use of expansion functions, of which there are two types in this work: Taylor Expansion functions (TE) and Lagrange Expansion functions (LE). The formulation was not formally influenced by the choice of theory, and this allows for an easy comparison between models by comparing lower and higher-order theories.

From the analysis cases presented, it was possible to draw some conclusions:

- The presented formulation allows for an accurate description of the equilibrium path and displacement response of beams with different cross-sections subjected to thermal loading, with the assumption of geometric nonlinearity, constant material properties, and perfect geometry.

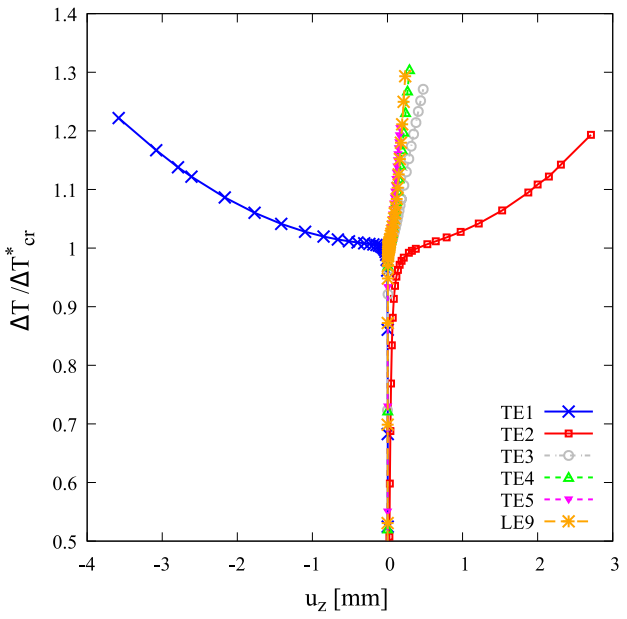


Fig. 21. u_z displacement against $\Delta\mathcal{T}/\Delta\mathcal{T}^*_{cr}$, calculated at the centre of the beam. Temperature value non-dimensionalised using the critical temperature reported in Table 6 with mark *. Evaluation of the influence of the Expansion theory, comparing TE and LE models. Analysis with discretisation fixed at 30B4. Titanium alloy C-section beam with uniform over-temperature and fixed constraints.

- In the description of highly slender square-section beams, the use of lower-order theories with the von Kármán nonlinearities is adequate to describe the nonlinear displacement of the beam. However, as the beam slenderness decreases, the shear effect becomes more significant, and the impact of the Green–Lagrange strain tensor, in combination with higher-order theories, becomes more evident, thus making these models necessary for a more complete description of the response.
- Linearised buckling analyses and nonlinear geometric analyses often yield different results. The comparison between linearised buckling analyses and nonlinear equilibrium paths shows that the mode associated with the lowest critical eigenvalue does not necessarily govern the post-buckling response. However, comparing these two analyses provides useful insights into the interpretation of the structural response output and into the ability of kinematic theories to capture or fail to capture certain phenomena.
- The post-buckling response clearly depends on the cross-sectional geometry. In the Z-beam, the nonlinear behaviour is dominated by torsional effects, while in the C-section, local modes arise.
- Lower-order Taylor expansion theories fail to accurately describe the post-buckling equilibrium path of beams with open cross-sections dominated by torsional or local-mode phenomena. The minimum theoretical order required to describe the behaviour, even qualitatively, depends on the geometry and the phenomenon being analysed. In the analysed cases, for a Z-section, torsion can be described using TE4 models, but the critical temperatures and displacement levels consistent with the Lagrange models are obtained using a TE10 model. For a C-section beam, the local phenomena are described by a TE3 model, but values similar to those of the LE9 model are obtained with a TE5 model.
- For beams with open cross-sections, the use of higher-order theories is necessary also to account for local phenomena associated with section deformation and warping-related effects, which play a relevant role in the nonlinear response.
- The presented results highlight that the minimum Taylor expansion order required for an adequate description of the structural response is not universal, but depends on the cross-sectional geometry and on the main mechanism involved in the post-buckled configuration.

The aim of this study was to develop a methodology for describing the nonlinear geometric and thermal post-buckling behaviour of beams using the CUF. Future work could focus on incorporating material nonlinearity and investigating equilibrium stability.

CRediT authorship contribution statement

Francesca Bracaglia: Writing – original draft, Visualization, Validation, Software, Investigation, Formal analysis. **Alfonso Pagani:** Writing – review & editing, Supervision, Resources, Methodology, Conceptualization. **Enrico Zappino:** Writing – review & editing, Supervision, Software, Methodology, Conceptualization. **Erasmo Carrera:** Writing – review & editing, Supervision, Methodology, Conceptualization.

Declaration of competing interest

The authors declare that they have no known competing financial interests or personal relationships that could have appeared to influence the work reported in this paper.

Acknowledgements

This research was funded by the Italian Ministry of University and Research (MUR) – Fondo Italiano per la Scienza (FIS 2), grant number FIS-00918 (Project AMPERE).

Appendix A. Differential operator

The present section collects the explicit formulation of the derivative operator of the Green Lagrange strain tensor. It is employed in the following geometrical relations:

$$\boldsymbol{\epsilon}_m = \boldsymbol{\epsilon}_l + \boldsymbol{\epsilon}_{nl} = \left(\boldsymbol{b}_l + \boldsymbol{b}_{nl}\right)\boldsymbol{u} \tag{A.1}$$

where $\boldsymbol{\epsilon}_m$ denotes the mechanical strain vector and the footnote l and nl are referred to the linear and nonlinear components respectively.

$$\boldsymbol{b}_l = \begin{pmatrix} \frac{\partial}{\partial x} & 0 & 0 \\ 0 & \frac{\partial}{\partial y} & 0 \\ 0 & 0 & \frac{\partial}{\partial z} \\ \frac{\partial}{\partial z} & 0 & \frac{\partial}{\partial x} \\ 0 & \frac{\partial}{\partial z} & \frac{\partial}{\partial y} \\ \frac{\partial}{\partial y} & \frac{\partial}{\partial x} & 0 \end{pmatrix} \qquad \boldsymbol{b}_{nl} = \begin{pmatrix} \frac{1}{2}\left(\frac{\partial}{\partial x}\right)^2 & \frac{1}{2}\left(\frac{\partial}{\partial x}\right)^2 & \frac{1}{2}\left(\frac{\partial}{\partial x}\right)^2 \\ \frac{1}{2}\left(\frac{\partial}{\partial y}\right)^2 & \frac{1}{2}\left(\frac{\partial}{\partial y}\right)^2 & \frac{1}{2}\left(\frac{\partial}{\partial y}\right)^2 \\ \frac{1}{2}\left(\frac{\partial}{\partial z}\right)^2 & \frac{1}{2}\left(\frac{\partial}{\partial z}\right)^2 & \frac{1}{2}\left(\frac{\partial}{\partial z}\right)^2 \\ \frac{\partial}{\partial x}\cdot\frac{\partial}{\partial z} & \frac{\partial}{\partial x}\cdot\frac{\partial}{\partial z} & \frac{\partial}{\partial x}\cdot\frac{\partial}{\partial z} \\ \frac{\partial}{\partial y}\cdot\frac{\partial}{\partial z} & \frac{\partial}{\partial y}\cdot\frac{\partial}{\partial z} & \frac{\partial}{\partial y}\cdot\frac{\partial}{\partial z} \\ \frac{\partial}{\partial x}\cdot\frac{\partial}{\partial y} & \frac{\partial}{\partial x}\cdot\frac{\partial}{\partial y} & \frac{\partial}{\partial x}\cdot\frac{\partial}{\partial y} \end{pmatrix} \tag{A.2}$$

where the symbol $\partial/\partial(\cdot)$ indicates the partial derivative.

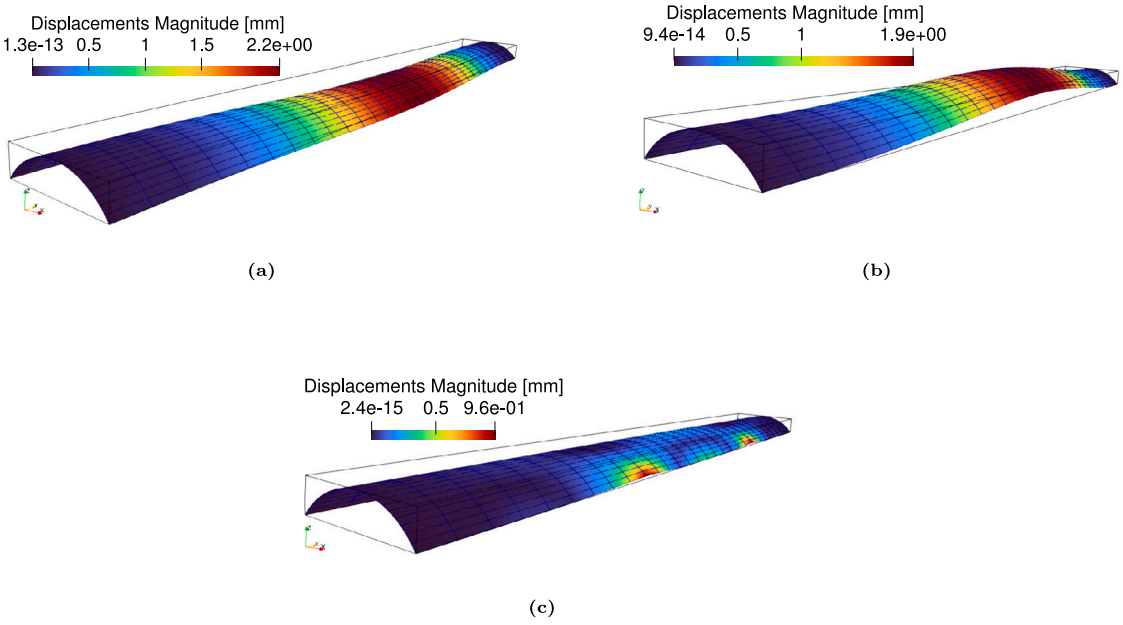


Fig. 22. Equilibrium displacement configuration, scale factor=1. Discretisation with 30B4 along the axis, (a) TE1 model at $\Delta T = 320$ °C, (b) TE2 model at $\Delta T = 320$ °C (c) LE9 model at $\Delta T = 70$ °C. Titanium alloy C-section beam with uniform over-temperature and fixed constraints.

Appendix B. Secant stiffness matrix nuclei

From the definition in Eq. (15) it is possible to write the first term as:

$$\begin{aligned}\int_V \delta\boldsymbol{\varepsilon}_m^T \boldsymbol{C}\boldsymbol{\varepsilon}_m dV &= \int_V \delta\left(\boldsymbol{\varepsilon}_l + \boldsymbol{\varepsilon}_{nl}\right)^T \boldsymbol{C}\left(\boldsymbol{\varepsilon}_l + \boldsymbol{\varepsilon}_{nl}\right) dV \\ &= \int_V \delta\boldsymbol{\varepsilon}_l^T \boldsymbol{C}\boldsymbol{\varepsilon}_l dV + \int_V \delta\boldsymbol{\varepsilon}_l^T \boldsymbol{C}\boldsymbol{\varepsilon}_{nl} dV + \int_V \delta\boldsymbol{\varepsilon}_{nl}^T \boldsymbol{C}\boldsymbol{\varepsilon}_l dV \\ &+ \int_V \delta\boldsymbol{\varepsilon}_{nl}^T \boldsymbol{C}\boldsymbol{\varepsilon}_{nl} dV\end{aligned} \tag{B.1}$$

From the definition of the internal virtual work and substituting CUF and FEM from Eq. (5), it is possible to obtain the following formulation:

$$\begin{aligned}\int_V \delta\boldsymbol{\varepsilon}_m^T \boldsymbol{C}\boldsymbol{\varepsilon}_m dV = &\int_V \delta\left(\boldsymbol{b}_l F_s(x,z) N_j(y) \boldsymbol{q}_{sj}\right)^T \boldsymbol{C}\left(\boldsymbol{b}_l F_\tau(x,z) N_i(y) \boldsymbol{q}_{\tau i}\right) dV + \\ &\int_V \delta\left(\boldsymbol{b}_l F_s(x,z) N_j(y) \boldsymbol{q}_{sj}\right)^T \boldsymbol{C}\left(\boldsymbol{b}_{nl} F_\tau(x,z) N_i(y) \boldsymbol{q}_{\tau i}\right) dV + \\ &\int_V \delta\left(\boldsymbol{b}_{nl} F_s(x,z) N_j(y) \boldsymbol{q}_{sj}\right)^T \boldsymbol{C}\left(\boldsymbol{b}_l F_\tau(x,z) N_i(y) \boldsymbol{q}_{\tau i}\right) dV + \\ &\int_V \delta\left(\boldsymbol{b}_{nl} F_s(x,z) N_j(y) \boldsymbol{q}_{sj}\right)^T \boldsymbol{C}\left(\boldsymbol{b}_{nl} F_\tau(x,z) N_i(y) \boldsymbol{q}_{\tau i}\right) dV\end{aligned} \tag{B.2}$$

where applying the differential operator on shape and expansion functions it is possible to obtain $\boldsymbol{B}_l$ and $\boldsymbol{B}_{nl}$. The FNs $\boldsymbol{B}_l^{\tau i}$ and $\boldsymbol{B}_{nl}^{\tau i}$ reported in Eqs. (B.3) and (B.4):

$$\boldsymbol{B}_l^{\tau i} = \boldsymbol{b}_l\left(F_\tau(x,z) N_i(y)\right) = \begin{bmatrix} F_{\tau,x} N_i & 0 & 0 \\ 0 & F_\tau N_{i,y} & 0 \\ 0 & 0 & F_{\tau,z} N_i \\ F_{\tau,z} N_i & 0 & F_{\tau,x} N_i \\ 0 & F_{\tau,z} N_i & F_\tau N_{i,y} \\ F_\tau N_{i,y} & F_{\tau,x} N_i & 0 \end{bmatrix} \tag{B.3}$$

$$\boldsymbol{B}_{nl}^{\tau i} = \boldsymbol{b}_{nl}\left(F_\tau(x,z) N_i(y)\right) = \frac{1}{2}\begin{bmatrix} u_{x,x} F_{\tau,x} N_i & u_{y,x} F_{\tau,x} N_i & u_{z,x} F_{\tau,x} N_i \\ u_{x,y} F_\tau N_{i,y} & u_{y,y} F_\tau N_{i,y} & u_{z,y} F_\tau N_{i,y} \\ u_{x,z} F_{\tau,z} N_i & u_{y,z} F_{\tau,z} N_i & u_{z,z} F_{\tau,z} N_i \\ u_{x,x} F_{\tau,z} N_i + u_{x,z} F_{\tau,x} N_i & u_{y,x} F_{\tau,z} N_i + u_{y,z} F_{\tau,x} N_i & u_{z,x} F_{\tau,z} N_i + u_{z,z} F_{\tau,x} N_i \\ u_{x,y} F_{\tau,z} N_i + u_{x,z} F_\tau N_{i,y} & u_{y,y} F_{\tau,z} N_i + u_{y,z} F_\tau N_{i,y} & u_{z,y} F_{\tau,z} N_i + u_{z,z} F_\tau N_{i,y} \\ u_{x,x} F_\tau N_{i,y} + u_{x,y} F_{\tau,x} N_i & u_{y,x} F_\tau N_{i,y} + u_{y,y} F_{\tau,x} N_i & u_{z,x} F_\tau N_{i,y} + u_{z,y} F_{\tau,x} N_i \end{bmatrix} \tag{B.4}$$

where the subscript ',' stands for the derivative. It is possible to demonstrate that $\delta(\boldsymbol{B}_l^{sj}\boldsymbol{q}_{sj}) = \boldsymbol{B}_l^{sj}\delta\boldsymbol{q}_{sj}$ $\delta(\boldsymbol{B}_{nl}^{sj}\boldsymbol{q}_{sj}) = 2\boldsymbol{B}_{nl}^{sj}\delta\boldsymbol{q}_{sj}$. Applying the virtual variation, Eq. (B.2) becomes as follows:

$$\begin{aligned}\int_V \delta\boldsymbol{\varepsilon}_m^T \boldsymbol{C}\boldsymbol{\varepsilon}_m dV &= \int_V \delta\boldsymbol{q}_{sj}^T \boldsymbol{B}_l^{sjT} \boldsymbol{C}\boldsymbol{B}_l^{\tau i}\boldsymbol{q}_{\tau i} dV + \int_V \delta\boldsymbol{q}_{sj}^T \boldsymbol{B}_l^{sjT} \boldsymbol{C}\boldsymbol{B}_{nl}^{\tau i}\boldsymbol{q}_{\tau i} dV + \\ &\int_V \delta\boldsymbol{q}_{sj}^T 2\boldsymbol{B}_{nl}^{sjT} \boldsymbol{C}\boldsymbol{B}_l^{\tau i}\boldsymbol{q}_{\tau i} dV + \int_V \delta\boldsymbol{q}_{sj}^T 2\boldsymbol{B}_{nl}^{sjT} \boldsymbol{C}\boldsymbol{B}_{nl}^{\tau i}\boldsymbol{q}_{\tau i} dV \\ &= \delta\boldsymbol{q}_{sj}^T \left[\boldsymbol{K}_0^{ij\tau s} + \boldsymbol{K}_{lnl}^{ij\tau s} + \boldsymbol{K}_{nll}^{ij\tau s} + \boldsymbol{K}_{nlnl}^{ij\tau s}\right] \boldsymbol{q}_{\tau i}\end{aligned} \tag{B.5}$$

Appendix C. Tangent stiffness matrix

The first terms of Eq. (30) are composed only by mechanical terms. The complete formulation is reported here.

$$\begin{aligned}\int_V \delta\boldsymbol{\varepsilon}_m^T \delta\boldsymbol{\sigma} dV &= \int_V \delta\boldsymbol{\varepsilon}_m^T \delta(\boldsymbol{\sigma}_m + \boldsymbol{\sigma}_\theta) dV = \int_V \delta\boldsymbol{\varepsilon}_m^T \delta\boldsymbol{\sigma}_m dV + \int_V \delta\boldsymbol{\varepsilon}_m^T \cancel{\delta\boldsymbol{\sigma}_\theta} dV \\ &= \int_V \delta(\boldsymbol{\varepsilon}_l + \boldsymbol{\varepsilon}_{nl})^T \delta(\boldsymbol{\sigma}_l + \boldsymbol{\sigma}_{nl}) dV \\ &= \int_V \delta(\boldsymbol{\varepsilon}_l + \boldsymbol{\varepsilon}_{nl})^T \boldsymbol{C}\delta(\boldsymbol{\varepsilon}_l + \boldsymbol{\varepsilon}_{nl}) dV \\ &= \int_V \delta\boldsymbol{\varepsilon}_l^T \boldsymbol{C}\delta\boldsymbol{\varepsilon}_l dV + \int_V \delta\boldsymbol{\varepsilon}_{nl}^T \boldsymbol{C}\delta\boldsymbol{\varepsilon}_l dV \\ &+ \int_V \delta\boldsymbol{\varepsilon}_l^T \boldsymbol{C}\delta\boldsymbol{\varepsilon}_{nl} dV + \int_V \delta\boldsymbol{\varepsilon}_{nl}^T \boldsymbol{C}\delta\boldsymbol{\varepsilon}_{nl} dV\end{aligned} \tag{C.1}$$

$$\boldsymbol{B}^{*}_{nl} = \begin{bmatrix} F_{\tau,x}N_iF_{s,x}N_j & F_{\tau,x}N_iF_{s,x}N_j & F_{\tau,x}N_iF_{s,x}N_j \\ F_{\tau}N_{i,y}F_sN_{j,y} & F_{\tau}N_{i,y}F_sN_{j,y} & F_{\tau}N_{i,y}F_sN_{j,y} \\ F_{\tau,z}N_iF_{s,z}N_j & F_{\tau,z}N_iF_{s,z}N_j & F_{\tau,z}N_iF_{s,z}N_j \\ F_{\tau,x}N_iF_{s,z}N_j + F_{\tau,z}N_iF_{s,x}N_j & F_{\tau,x}N_iF_{s,z}N_j + F_{\tau,z}N_iF_{s,x}N_j & F_{\tau,x}N_iF_{s,z}N_j + F_{\tau,z}N_iF_{s,x}N_j \\ F_{\tau}N_{i,y}F_{s,z}N_j + F_{\tau,z}N_iF_sN_{j,y} & F_{\tau}N_{i,y}F_{s,z}N_j + F_{\tau,z}N_iF_sN_{j,y} & F_{\tau}N_{i,y}F_{s,z}N_j + F_{\tau,z}N_iF_sN_{j,y} \\ F_{\tau,x}N_iF_sN_{j,y} + F_{\tau}N_{i,y}F_{s,x}N_j & F_{\tau,x}N_iF_sN_{j,y} + F_{\tau}N_{i,y}F_{s,x}N_j & F_{\tau,x}N_iF_sN_{j,y} + F_{\tau}N_{i,y}F_{s,x}N_j \end{bmatrix} \tag{C.6}$$

Box III.

Substituting Eqs. (9) and (10) in Eq. (C.1) and considering the derivative rules for matrix $\boldsymbol{B}$, it is possible to define the components of the tangent matrix described in the first part of Eq. (30) in terms of FNs.

$$\int_V \delta\boldsymbol{\varepsilon}_l^T\boldsymbol{C}\delta\boldsymbol{\varepsilon}_l dV = \delta\boldsymbol{q}_{s\tau}^T\int_V \boldsymbol{B}_l^{sjT}\boldsymbol{C}\boldsymbol{B}_l^{\tau i}dV\delta\boldsymbol{q}^{\tau i} = \delta\boldsymbol{q}_{sj}^T\boldsymbol{K}_0^{ij\tau s}\delta\boldsymbol{q}_{\tau i} \tag{C.2}$$

$$\int_V \delta\boldsymbol{\varepsilon}_{nl}^T\boldsymbol{C}\delta\boldsymbol{\varepsilon}_l dV = \delta\boldsymbol{q}_{s\tau}^T\int_V 2\boldsymbol{B}_{nl}^{sjT}\boldsymbol{C}\boldsymbol{B}_l^{\tau i}dV\delta\boldsymbol{q}^{\tau i} = \delta\boldsymbol{q}_{sj}^T\boldsymbol{K}_{nll}^{ij\tau s}\delta\boldsymbol{q}_{\tau i} \tag{C.3}$$

$$\int_V \delta\boldsymbol{\varepsilon}_l^T\boldsymbol{C}\delta\boldsymbol{\varepsilon}_{nl} dV = \delta\boldsymbol{q}_{s\tau}^T\int_V \boldsymbol{B}_l^{sjT}\boldsymbol{C}2\boldsymbol{B}_{nl}^{\tau i}dV\delta\boldsymbol{q}^{\tau i} = \delta\boldsymbol{q}_{sj}^T2\boldsymbol{K}_{lnl}^{ij\tau s}\delta\boldsymbol{q}_{\tau i} \tag{C.4}$$

$$\int_V \delta\boldsymbol{\varepsilon}_{nl}^T\boldsymbol{C}\delta\boldsymbol{\varepsilon}_{nl} dV = \delta\boldsymbol{q}_{s\tau}^T\int_V 2\boldsymbol{B}_{nl}^{sjT}\boldsymbol{C}2\boldsymbol{B}_{nl}^{\tau i}dV\delta\boldsymbol{q}^{\tau i} = \delta\boldsymbol{q}_{sj}^T2\boldsymbol{K}_{nlnl}^{ij\tau s}\delta\boldsymbol{q}_{\tau i} \tag{C.5}$$

where the components of the tangent stiffness matrix are the same as the one in Eq. (B.5).

The application of the second-order variation and the explicit formulation of the second variation of strains are not reported here but can be found in [34]. With some simple manipulations, it is possible to express $\delta^2\boldsymbol{\varepsilon}_{nl}$ vector as the combination of the matrix $\boldsymbol{B}^{*}_{nl}$ reported in Eq. (C.6) and a vector with the product of the virtual variations of nodal unknowns as expressed in Eq. (C.7) (see the equation in Box III). In the present matrix, F_τ and F_s denote the expansion functions, N_i and N_j are referred to as the shape functions and the subscript ',' stands for the derivative.

$$\delta^2\boldsymbol{\varepsilon}_{nl} = \boldsymbol{B}^{*}_{nl}\begin{Bmatrix} \delta q_{x_{\tau i}}\delta q_{x_{sj}} \\ \delta q_{y_{\tau i}}\delta q_{y_{sj}} \\ \delta q_{z_{\tau i}}\delta q_{z_{sj}} \end{Bmatrix} \tag{C.7}$$

The second part of the tangent stiffness matrix can be obtained in terms of FNs:

$$\int_V \delta^2\boldsymbol{\varepsilon}_{nl}^T\boldsymbol{\sigma}dV = \int_V\left(\boldsymbol{B}^{*}_{nl}\begin{Bmatrix} \delta q_{x_{\tau i}}\delta q_{x_{sj}} \\ \delta q_{y_{\tau i}}\delta q_{y_{sj}} \\ \delta q_{z_{\tau i}}\delta q_{z_{sj}} \end{Bmatrix}\right)^T\boldsymbol{\sigma}dV$$

$$= \int_V\left(\boldsymbol{B}^{*}_{nl}\begin{Bmatrix} \delta q_{x_{\tau i}}\delta q_{x_{sj}} \\ \delta q_{y_{\tau i}}\delta q_{y_{sj}} \\ \delta q_{z_{\tau i}}\delta q_{z_{sj}} \end{Bmatrix}\right)^T\left(\boldsymbol{\sigma}_l + \boldsymbol{\sigma}_{nl} + \boldsymbol{\sigma}_\theta\right)dV =$$

$$\delta\boldsymbol{q}_{sj}^T\int_V diag\left(\boldsymbol{B}^{*T}_{nl}(\boldsymbol{\sigma}_l + \boldsymbol{\sigma}_{nl} + \boldsymbol{\sigma}_\theta)\right)dV\delta\boldsymbol{q}_{\tau i}$$

$$= \delta\boldsymbol{q}_{sj}^T\left[\boldsymbol{K}_{\sigma l}^{ij\tau s} + \boldsymbol{K}_{\sigma nl}^{ij\tau s} + \boldsymbol{K}_{\sigma\theta}^{ij\tau s}\right]\delta\boldsymbol{q}_{\tau i} = \delta\boldsymbol{q}_{sj}^T\left[\boldsymbol{K}_{\sigma}^{ij\tau s} + \boldsymbol{K}_{\sigma\theta}^{ij\tau s}\right]\delta\boldsymbol{q}_{\tau i} \tag{C.8}$$

Data availability

Data will be made available on request.

References

[1] E.A. Thornton, D.B. Paul, Thermal-structural analysis of large space structures - an assessment of recent advances, J. Spacecr. Rockets 22 (4) (1985) 385–393.

[2] W. Guo, Y. Li, Y.Z. Li, S. Tian, S. Wang, Thermal–structural analysis of large deployable space antenna under extreme heat loads, J. Therm. Stresses 39 (8) (2016) 887–905.

[3] H. Zhang, X. Zhao, Q. Mei, Y. Wang, S. Song, F. Yu, On-orbit thermal deformation prediction for a high-resolution satellite camera, Appl. Therm. Eng. 195 (2021) 117152.

[4] J. Hedgepeth, Critical requirements for the design of large space structures, in: 2nd Conference on Large Space Platforms: Toward Permanent Manned Occupancy in Space, American Institute of Aeronautics and Astronautics, 1981.

[5] U. Lee, Dynamic continuum modeling of beamlike space structures using finite-element matrices, AIAA J. 28 (4) (1990) 725–731.

[6] R.B. Hetnarski, M.R. Eslami, Thermal Stresses—Advanced Theory and Applications, Springer International Publishing, 2019.

[7] B.V. Sankar, J.T. Tzeng, Thermal stresses in functionally graded beams, AIAA J. 40 (6) (2002) 1228–1232.

[8] G. Giunta, N. Metla, S. Belouettar, AJM. Ferreira, E. Carrera, A thermo-mechanical analysis of isotropic and composite beams via collocation with radial basis functions, J. Therm. Stresses 36 (11) (2013) 1169–1199.

[9] E. Carrera, F.A. Fazzolari, M. Cinefra, Thermal Stress Analysis of Composite Beams, Plates and Shells, Joe Hayton, Amsterdam, 2017.

[10] S.R. Li, R.C. Batra, Thermal buckling and postbuckling of Euler-Bernoulli beams supported on nonlinear elastic foundations, AIAA J. 45 (3) (2007) 712–720.

[11] T.C. Mathew, G.R. Singh, G.V. Rao, Thermal buckling of cross-ply composite laminates, Comput. Struct. 42 (2) (1992) 281–287.

[12] Y. Yan, A. Pagani, E. Carrera, Thermal buckling solutions of generic metallic and laminated structures: Total and updated Lagrangian formulations via refined beam elements, J. Therm. Stresses 45 (8) (2022) 669–694.

[13] A. Derbale, M. Bouazza, N. Benseddiq, Analysis of the mechanical and thermal buckling of laminated beams by new refined shear deformation theory, Iran. J. Sci. Technol. Trans. Civ. Eng. 45 (1) (2020) 89–98.

[14] C. Wen, L. Tang, G. Yang, Buckling and post-buckling of pinned Euler beams on weakened Winkler foundation under thermal loading, J. Therm. Stresses 43 (5) (2020) 529–542.

[15] G. Yang, M.A. Bradford, Thermal-induced buckling and postbuckling analysis of continuous railway tracks, Int. J. Solids Struct. 97–98 (2016) 637–649.

[16] S. Li, Y.H. Zhou, X. Zheng, Thermal post-buckling of a heated elastic rod with pinned-fixed end, J. Therm. Stresses 25 (1) (2002) 45–56.

[17] S. Li, Y. Zhou, Geometrically nonlinear analysis of timoshenko beams under thermomechanical loadings, J. Therm. Stresses 26 (9) (2003) 861–872.

[18] S. Li, X. Song, Large thermal deflections of timoshenko beams under transversely non-uniform temperature rise, Mech. Res. Commun. 33 (1) (2006) 84–92.

[19] X. Li, K. Yu, R. Zhao, Thermal post-buckling and vibration analysis of a symmetric sandwich beam with clamped and simply supported boundary conditions, Arch. Appl. Mech. 88 (4) (2017) 543–561.

[20] M.A. Vaz, J.C.R. Cyrino, A.C. Neves, Initial thermo-mechanical post-buckling of beams with temperature-dependent physical properties, Int. J. Non-Linear Mech. 45 (3) (2010) 256–262.

[21] Y. Fu, J. Wang, S. Hu, Analytical solutions of thermal buckling and postbuckling of symmetric laminated composite beams with various boundary conditions, Acta Mech. Eometrically Nonlinear Analysis of Timoshenko Beams Under Thermomechanical Loadings 225 (1) (2013) 13–29.

[22] N. George, P. Jeyaraj, S.M. Murigendrappa, Buckling of non-uniformly heated isotropic beam: Experimental and theoretical investigations, Thin-Walled Struct. 108 (2016) 245–255.

[23] G. She, F. Yuan, Y. Ren, Thermal buckling and post-buckling analysis of functionally graded beams based on a general higher-order shear deformation theory, Appl. Math. Model. 47 (2017) 340–357.

[24] M. Amabili, An accurate model for nonlinear forced vibrations of higher-order and timoshenko cantilever beams, Compos. Struct. 381 (2026) 120035.

[25] M. Amabili, G. Ferrari, M.H. Ghayesh, C. Hameury, H. Hena Z., Nonlinear vibrations and viscoelasticity of a self-healing composite cantilever beam: Theory and experiments, Compos. Struct. 294 (2022) 115741.

[26] A. Pagani, P. Chiaia, E. Carrera, Vibration of solid and thin-walled slender structures made of soft materials by high-order beam finite elements, Int. J. Non-Linear Mech. 160 (2024) 104634.

[27] Z.Z. Liu, J.L. Huang, An improved high-order finite element method for nonlinear vibration of a rotating flexible hub-beam, Int. J. Non-Linear Mech. 182 (2026) 105308.

[28] X. Chen, H. Wu, G. Nie, A robust isogeometric nonlinear analysis framework with branch-switching functionality for bifurcation, localization and mode interaction of variable-stiffness sandwich beams under compression, Int. J. Non-Linear Mech. 179 (2025) 105217.
[29] E. Carrera, G. Giunta, Refined beam theories based on a unified formulation, Int. J. Appl. Mech. 02 (01) (2010) 117–143.
[30] E. Carrera, E. Zappino, M. Cinefra, M. Petrolo, Finite Element Analysis of Structures Through Unified Formulation, Wiley, Chichester, West Sussex, 2014.
[31] T. Taki, Optimization of flat Z-stiffened panel subjected to compression, Trans. Japan Soc. Aeronaut. Space Sci. 62 (1) (2019) 44–54.
[32] S.J. Thaker, H. Arora, D.B. Shah, Tape spring for deployable space structures: A review, Adv. Space Res. 73 (10) (2024) 5188–5219.
[33] S.S. Rao, The Finite Element Method in Engineering, Elsevier, Amsterdam, 2011.
[34] A. Pagani, E. Carrera, Unified formulation of geometrically nonlinear refined beam theories, Mech. Adv. Mater. Struct. 25 (1) (2016) 15–31.
[35] J.N. Reddy, An Introduction to Nonlinear Finite Element Analysis, Second ed., first published in paperback ed., Oxford University Press, Oxford, 2020.
[36] M.A. Crisfield, An arc-length method including line searches and accelerations, Internat. J. Numer. Methods Engrg. 19 (9) (1983) 1269–1289.
[37] E. Carrera, A study on arc-length-type methods and their operation failures illustrated by a simple model, Comput. Struct. 50 (2) (1994) 217–229.
[38] S.D. Akbas, T. Kocaturk, Post-buckling analysis of a simply supported beam under uniform thermal loading, Sci. Res. Essays Vol. 6(4) (4) (2011) 1135–1142.
[39] A. Pagani, E. Carrera, R. Augello, Evaluation of various geometrical nonlinearities in the response of beams and shells, AIAA J. 57 (8) (2019) 3524–3533.
[40] A. Pagani, F. Bracaglia, E. Zappino, E. Carrera, Nonlinear thermal stresses analysis and post-buckling of rectangular composite laminates using high-order plate finite elements, J. Therm. Stresses (2026) 1–27.
[41] P. Chiaia, A. Pagani, E. Carrera, Large strain and 3D stress analysis of laminated fiber-reinforced soft material structures with high order beam finite elements, Comput. Struct. 313 (2025) 107735.
[42] F. Bracaglia, R. Masia, A. Pagani, E. Zappino, E. Carrera, Thermal buckling of variable stiffness composite laminates using high order plate finite elements, Compos. Struct. 345 (2024) 118393.
[43] S.M. Ibrahim, E. Carrera, M. Petrolo, E. Zappino, Buckling of thin-walled beams by a refined theory, J. Zhejiang Univ. Science A 13 (10) (2012) 747–759.